Secondary instability of crossflow vortices

By EDWARD B. WHITE[1] AND WILLIAM S. SARIC[2]

[1]Case Western Reserve University, Cleveland, OH 44106, USA

[2]Texas A&M University, TX 77843, USA

Crossflow-dominated swept-wing boundary layers are known to undergo a highly nonlinear transition process. In low-disturbance environments, the primary instability of these flows consists mainly of stationary streamwise vortices that modify the mean velocity field and hence the stability characteristics of the boundary layer. The result is amplitude saturation of the dominant stationary mode and strong spanwise modulation of the unsteady modes. Breakdown is not caused by the primary instability but instead by a high-frequency secondary instability of the shear layers of the distorted mean flow. The secondary instability has been observed in several previous experiments and several computational models for its behaviour exist. None of the experiments has been sufficiently detailed to allow either model validation or transition correlation. The present experiment conducted using a 45° swept wing in the low-disturbance Arizona State University Unsteady Wind Tunnel addresses the secondary instability in a detailed fashion under a variety of conditions. The results reveal that this instability is active in the breakdown of all cases investigated, and furthermore, it appears to be well-described by the computational models.

1. Introduction

Understanding laminar-to-turbulent transition of crossflow-dominated swept-wing boundary layers represents a challenging problem of significant technological importance. The primary instability of these boundary layers originates from the inflectional velocity profile of a secondary flow called crossflow. Crossflow exists due to the combined influences of sweep and pressure gradient that generate curved inviscid streamlines at the boundary-layer edge. Inside the boundary layer the velocity is reduced but the pressure gradient is unchanged relative to the external flow, and the resulting imbalance produces crossflow perpendicular to the inviscid streamline, towards its centre of curvature. A schematic of the streamwise and crossflow velocity components is given in figure 1. Because the unstable component of the basic flow is perpendicular to the inviscid streamlines, the instability is primarily manifested as vortices oriented within a few degrees of the streamwise direction. Linear stability theory indicates that both stationary and travelling disturbances are unstable but that travelling waves are the most amplified. However, because the initial amplitudes of stationary waves are much stronger than those of travelling waves under conditions of low turbulence intensity, and because of the ability of the stationary waves to produce a strong integrated disturbance, stationary waves usually dominate transition in free-stream environments characteristic of flight.

The presence of amplified stationary vortices is critically important for the stability behaviour of crossflow boundary layers. Despite being rather weak, the integrated
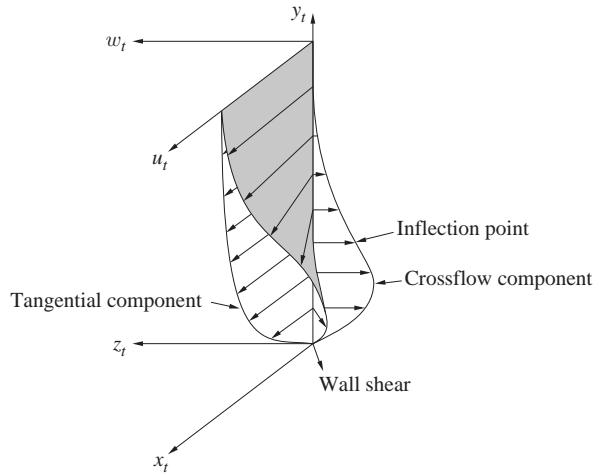
FIGURE 1. Crossflow boundary-layer velocity profiles.

effect of the steady v', w' velocity disturbances produces very significant mean-flow distortion. The result is saturation of the primary instability at 10% to 30% amplitude. The distortion of the mean flow stabilizes the primary disturbance. This primary-instability behaviour has been the subject of very intense study over the past fifteen years and is now very well-understood. The principal experimental work of this period was carried out by Saric and coworkers at the Arizona State University Unsteady Wind Tunnel using a swept-wing model and by Bippes and coworkers at DLR in Göttingen using a swept flat plate and an external pressure body. A historical review of the crossflow problem is given by Reed & Saric (1989) and reviews of more recent developments are by Bippes (1999) and Saric, Reed & White (2003). Other related reviews are by Kachanov (1996), Arnal (1997), Crouch (1997), Herbert (1997a,b), and Reshotko (1997).

Although the primary instability is well-understood, the process by which the saturated vortices produced by this instability break down and lead to turbulence is not nearly as well-documented. What is observed in stationary-wave-dominated transition experiments is that, at some point aft of where the vortices saturate, breakdown to turbulence occurs very rapidly along a jagged front. This behaviour is particularly well-illustrated in flow-visualization studies such as that by Dagenhart & Saric (1999). These studies suggest that the final stage of transition occurs over a very short streamwise distance and that turbulence originates at fixed, distinct points in the boundary layer from which it spreads in a characteristic wedge pattern.

The scenario that most is likely to describe saturated-vortex breakdown is that the distorted mean flow produced by these vortices includes very strong and inflectional shear layers and thus becomes unstable to secondary instabilities. These instabilities grow to large amplitudes over a very short streamwise distance and lead to breakdown and turbulence. The first suggestion that this is the case was by Kohama (1987), who predicted that this mechanism (previously observed by Kohama 1984, 1985) in rotating-disk and cone boundary layers would be active in crossflow-dominated swept-wing boundary layers as well. Hot-wire measurements performed on a swept cylinder by Poll (1985) showed an intermittent velocity fluctuation at 17.5 kHz just upstream of the transition location in a boundary layer whose most unstable travelling crossflow waves were at 1.1 kHz. Poll attributed the high-frequency fluctuations to

intermittent turbulence, but Kohama (1987) argued that these fluctuations were in fact evidence of a high-frequency secondary instability.

To demonstrate that a high-frequency secondary instability is responsible for breakdown in swept-wing flows, Kohama, Saric & Hoos (1991) used hot-wire and flow-visualization studies to make a correlation between velocity-fluctuation spectra and the stationary structures revealed by flow visualizations. That experiment featured hot-wire scans taken at constant height, y, across a range of span locations. The measurements obtained at $x/c = 0.40$ on a 45° swept wing at $Re_c = 2.66 \times 10^6$ showed travelling crossflow wave activity at 350 Hz and a broad high-frequency peak at 3 kHz (Re_c being the Reynolds number based on chord, c). The spanwise scans showed that the amplitude of each frequency band varied significantly over each wavelength of the stationary disturbance and that the high-frequency disturbances grow rapidly in the stream direction just upstream of breakdown. The experiment provided good evidence that a secondary instability was active, but certain problems in the approach, most notably the absence of any full-field scans in the y- and z-directions and poor interpretations of the velocity-fluctuation spectra, meant that the results could not be used to support a general theory regarding the destabilization of the stationary vortices to secondary instabilities.

During the decade following the experiment by Kohama *et al.* (1991), there were several computational approaches taken to understand the secondary instability, and several experiments were performed that corrected many of the shortcomings of the Kohama *et al.* (1991) experiment. The most recent computations of secondary instability behaviour have been performed by Malik *et al.* (1999) using a two-dimensional eigenvalue approach; Koch *et al.* (2000) and Janke & Balakumar (2000) using a Floquet approach; and Högberg & Henningson (1998) and Wassermann & Kloker (2002) using direct numerical simulations of the breakdown region. Earlier computational efforts are described in those references, with an especially thorough treatment provided by Koch *et al.* (2000). The consensus of these efforts is that once the primary disturbance saturates, secondary instabilities are destabilized and grow extremely rapidly. The computations identify many different secondary-instability modes that are classified into two distinct categories based on the production mechanism. Type-I, or z, modes are produced by the spanwise gradients of the streamwise flow (i.e. $\partial U/\partial z$) and are usually the most amplified and lowest frequency modes of the secondary instabilities. Type-II, or y, modes are produced by wall-normal gradients (i.e. $\partial U/\partial y$), usually occur at higher frequencies than the type-I modes, and have a lower growth rate. The type-I and type-II nomenclature was introduced by Malik, Li & Chang (1996). This classification is generally applied by examining the location of the fluctuations of a particular frequency band relative to the stationary structure to identify the shear layer, $\partial U/\partial z$ or $\partial U/\partial y$, that is the more important production mechanism of the mode.

The experiments that followed the work by Kohama *et al.* (1991) were by Kohama, Onodera & Egami (1996), who examined two-dimensional disturbance fields and presented growth results of the secondary modes from a swept-flat-plate experiment. That effort was followed by Kawakami, Kohama & Okutsu (1999), who presented spectra, fluctuation-amplitude contour maps, and secondary-instability growth curves. Additionally, Kawakami *et al.* (1999) used a speaker located below a small hole in the plate to excite the flow at high frequencies and tracked the growth of the secondary instabilities of particular frequencies. In another series of experiments by Lerche & Bippes (1996) and Lerche (1996) at DLR, the secondary instability was observed in boundary layers in which a combination of travelling and stationary primary

disturbances was forced by variable leading-edge roughness. In those experiments, secondary-instability fluctuations were only observed for certain combinations of the travelling and stationary primary waves, suggesting that under some conditions neither the stationary nor travelling primary-instability waves are sufficiently strong to destabilize the secondary instability, but that superposition of both is capable of producing sufficient mean-flow deformation to destabilize the secondary instability for certain phase ranges of the superposition.

The experiments described above are in general agreement with the computational results. However, there has not yet been an experiment that provides a comprehensive examination of secondary-instability behaviour under a variety of carefully controlled conditions that is suitable for computational validation. It is the objective of the present work to provide detailed measurements of the secondary instability with particular attention paid to the correlation of secondary-instability behaviour and the underlying mean-flow structure. The objective is to validate the computational approaches and to provide additional data that can be incorporated into a crossflow transition prediction scheme. The facility, model, and approach used in the experiment are described in detail in §2, results of the secondary-instability measurements are given in §3, and conclusions are discussed in §4.

2. Experimental setup and measurement techniques

2.1. *Wind tunnel and swept-wing model*

The present experiment is the last of a series at the ASU Unsteady Wind Tunnel involving the stability of crossflow-dominated swept-wing boundary layers. It is to the great advantage of the current work to have inherited much of the approach and physical setup from the previous experiments of Dagenhart & Saric (1999), Radeztsky, Reibert & Saric (1999), Reibert *et al.* (1996), Saric, Carrillo & Reibert (1998), and Chapman *et al.* (1998). However, the swept-wing model used in all of the previous experiments has been replaced with a new model that incorporates a modular leading edge and provides a somewhat more advantageous pressure contour. Both swept-wing models share a design philosophy that has its origins with the work of Dagenhart & Saric (1999). The idea is to create an experimental platform that captures all of the essential features of a swept wing that undergoes crossflow-dominated transition and yet provides the simplest possible experimental and computational problem. If all of the important physics are included in the experiment and good agreement with computations is achieved, then the validated computations can be used with confidence to obtain results with more realistic operating conditions. This implies that, despite its additional complexity, a swept wing is preferable to a swept plate because wings provide surface curvature, and the results of nonlinear parabolized stability equation (NPSE) calculations by Haynes & Reed (2000) indicate that even though the curvature is quite small, it is an essential element for correctly predicting stationary-mode growth rates. The experimental model is not tapered, so a spanwise-uniform basic state can be established, greatly simplifying both the experiment and the stability calculations. Taper could be included in stability calculations, of course, but if those calculations indicated that taper influences the stability behaviour, that discovery would require a different model for validation. Without an indication that this could occur, and if so, for what parameter range, there is no reason to make the experiment more complicated than necessary.

The setup must provide boundary layers that are sufficiently thick to permit relatively easy and well-resolved boundary-layer velocity measurements and simultaneously provide sufficient crossflow to cause transition. These are contradictory
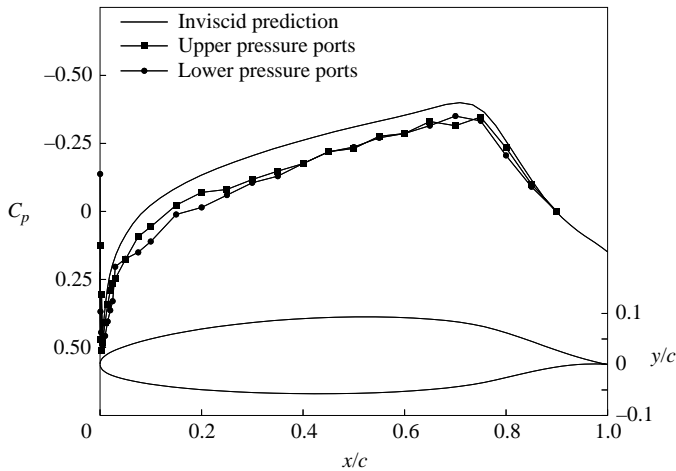
FIGURE 2. Airfoil shape, suction-side pressure distribution, and surface pressure measurements for the ASU(67)-0315 airfoil at $Re_c = 2.4 \times 10^6$ and $-3°$ angle of attack.

requirements because thick boundary layers can be achieved by restricting the experiment to low Reynolds numbers, but at too low a Reynolds number the instability is not strong enough to produce transition. One means of improving the prospect for strong crossflow and a thick boundary layer is selecting a pressure gradient that locates the pressure minimum as far aft as possible, permitting the boundary layer to develop over the longest possible distance without becoming unstable to Tollmien–Schlichting (T–S) waves. Crossflow is also enhanced by making the pressure gradient as strong as possible. Although this means that strong negative lift is preferable, experience at the Unsteady Wind Tunnel has shown that the wall liners used to maintain spanwise-uniform flow are difficult to construct and maintain when there is strong lift. The liner design and construction techniques are thoroughly documented by Dagenhart & Saric (1999) and Radeztsky (1994). Therefore, a pressure contour that provides a strong pressure gradient with a late pressure minimum at zero lift is the optimum configuration. Enhanced crossflow can also be produced by increasing the sweep angle of the wing. However, exceeding 45° sweep is impractical for the hot-wire traverse system.

The wing used in the current work, designated the ASU(67)-0315, was designed by M. S. Reibert around these principles. Its chord length parallel to the free stream is 1.83 m; its sweep angle is 45°; and its zero-lift angle is $-3°$. The wing's cross-section in a plane perpendicular to the leading edge is shown in figure 2. This figure also shows the theoretical inviscid pressure contour. Pressures are computed using a panel code that includes the influence of the wind-tunnel walls but not displacement thickness growth. After the wing was installed, a keyway in its mounting shaft was found to have been machined incorrectly. Because of this problem, the wing is not at the $-3°$ design position during the experiments, but instead is at $-3.4°$.

The extent to which the model and liners produce the conditions predicted by the inviscid code can be assessed by comparing the pressure measured using the surface pressure taps to the pressure distribution that is shown in figure 2. The measurements are for the actual $-3.4°$ angle of attack, but the computed curve reflects the design angle, $-3°$, for which the liners were constructed. (Results for $Re_c = 2.0 \times 10^6$ and

$Re_c = 2.8 \times 10^6$ are nearly indistinguishable from those given here.) The actual pressure is higher than the predicted value at all points upstream of 90% chord. However, the pressure gradient – the feature that affects boundary-layer stability – is very close to what is predicted by the panel code throughout the region of interest for the experiments, $0.30 < x/c < 0.60$. Furthermore, there is not an appreciable pressure difference across the span in this region.

The pressure results are quite similar to those obtained in previous ASU experiments (see figure 2 of Reibert *et al.* 1996) and indicate that the angle-of-attack defect, while unfortunate, does not produce any grossly incorrect behaviour. This should not be taken to mean that the transition location is insensitive to small angle-of-attack changes. A setting of $-3°$ would certainly produce slightly different results than those described below. Instead, it appears that the wall liners are not so sensitive to angle-of-attack variations that the $0.4°$ error produces significant spanwise non-uniformity. The role of the wall liners is to ensure spanwise-uniform flow and this appears to have been achieved. This result along with the exceptionally good agreement between Reibert *et al.*'s (1996) experimental results and the computations of Haynes & Reed (2000) indicates that the experiment can proceed with these pressure contours.

The ASU(67)-0315 wing was constructed to provide a flexible test platform on which a variety of boundary-layer transition-control experiments can be conducted. To this end, the leading edge of the wing is not continuous, but includes a leading-edge slot in the middle third of the span that extends to approximately 20% chord. This slot accepts modular leading-edge inserts that can provide any sort of boundary-layer treatment. The leading 10% chord of the main body of the model is a solid aluminium piece, hand polished to a 0.2-μm-r.m.s. surface finish. The leading-edge insert used for the current work is constructed of a solid aluminium piece machined to match the contour of the main body of the wing and to provide an exact fit at the junction between the insert and the main body. The surface of the insert is hand polished to the same 0.2-μm finish as the main body's leading edge. The remainder of the main body consists of an aluminium frame and foam core covered by fibreglass. Because of the large spanwise extent of the insert, its corners (which are sources of small-scale roughness) are far enough from the measurement region so the crossflow waves generated there do not affect the measurement region. This is confirmed with a naphthalene flow visualization test.

The ASU Unsteady Wind Tunnel is a closed-loop, low-speed, atmospheric-pressure facility designed to provide the best possible conditions for conducting transition-to-turbulence experiments. With this in mind, quite a significant investment has been made in high-quality screens, honeycomb, settling chamber, contraction cone, turning vanes, and vibration-isolation strategies. Details of the facility's design and capabilities are given by Saric (1992). The baseline operating point for the current experiment is $Re_c = 2.4 \times 10^6$, and for the temperatures at which the tunnel operates, this corresponds to free-stream speeds between 22 and 23 m s^{-1}. The baseline Reynolds number provides the best combination of experimental parameters. Breakdown occurs near 50% chord, in the middle of the traverse's range, and the boundary layer is reasonably thick (3 mm) in the transition region, so well-resolved boundary-layer profiles are easy to obtain. Wind-tunnel heating is a concern at this speed because the tunnel does not include a heat exchanger, but the heating is not so severe as to be unmanageable. The free-stream-turbulence level that is achieved in the test section is exceptionally low due to the attention that is paid to turbulence-control devices

and vibration control. At 20 m s^{-1}, the turbulence level u'/U_∞ is less than 0.02% (using a 2 Hz high-pass filter). Both the v' and w' fluctuation levels are less than half that of u'. The sound level in the test section at the same conditions is below 85 dB. Because Deyhle & Bippes (1996) found that stationary waves dominate crossflow boundary layers only below $Tu = 0.15\%$, the low turbulence level of the Unsteady Wind Tunnel is essential for conducting a stationary-wave-dominated experiment. Because the tunnel does not feature a heat exchanger, the speed is adjusted regularly to maintain a constant chord Reynolds number and the hot-wire calibration includes a sophisticated temperature compensation.

A high-precision, computer-controlled traverse mechanism is situated outside the front wall of the test section with access to the suction side of the wing. The resolutions in the various coordinate directions are $\Delta X = 12$ μm (stream direction), $\Delta Y = 0.7$ μm (wall-normal direction), and $\Delta Z = 1.3$ μm (unswept-span direction). The traverse is designed so that only the sting extends into the test section; the traverse mechanism is enclosed in a pressure box outside the test section. The sting is designed to allow the boundary-layer hot-wire probe support to be rotated toward the wing so that the sting itself need not be close to the wing. Additionally, the boundary-layer hot-wire can be rotated about the probe-support axis so that the hot-wire can be positioned parallel to the wing surface.

2.2. *Measurement techniques*

The instruments used to obtain the mean- and fluctuating-velocity measurements are constant-temperature hot-wire anemometers. Although a variety of more modern systems exists, hot-wires provide a number of features that make them ideal for boundary-layer-stability measurements. These include excellent spatial resolution in the wall-normal direction and the ability to high-pass filter and amplify the anemometer output so that accurate measurements of small, fluctuating-velocity components – exactly the feature of interest in stability measurements – can be effectively measured. There is always some concern that introduction of a flow-intrusive device such as a hot-wire can change the behaviour of a system being studied. This is especially true for stability experiments where very small influences can become quite significant. For the present experiment, this need not be a concern for several reasons. First, extensive naphthalene-flow-visualization experiments of the previous investigators (Dagenhart & Saric 1999; Radeztsky *et al.* 1999; Reibert *et al.* 1996) show that hot-wire measurements correspond exactly to behaviour indicated by the flow visualizations, for which no intrusive devices exist. Second, there is excellent correlation between the experimental results of Reibert *et al.* (1996) and the computational results of Haynes & Reed (2000), so there is additional reason to believe that the boundary-layer behaviour is unchanged by the presence of a boundary-layer hot-wire. Finally, in the breakdown region the instability mechanism is driven by an inviscid instability that does not depend on the pressure gradient (the feature of the flow that would be modified by the presence of the hot-wire and sting) but instead depends on the shear layer that is established by the stationary crossflow waves well upstream of the transition location.

Fluctuating-velocity components are the principal interest of this experiment, but the correlation of the fluctuating components to the underlying mean flow is also important. This means that a careful mean-flow calibration procedure is required that must include an accurate temperature compensation. The calibration procedure is performed daily to minimize long-term variations in the hot-wire response. The calibration approach is described in detail by White (2000).
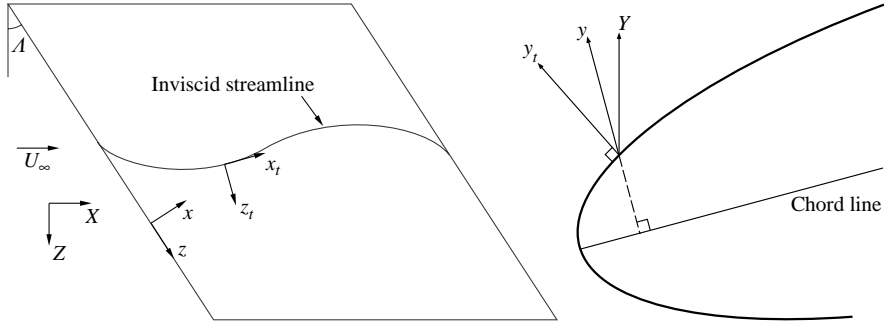
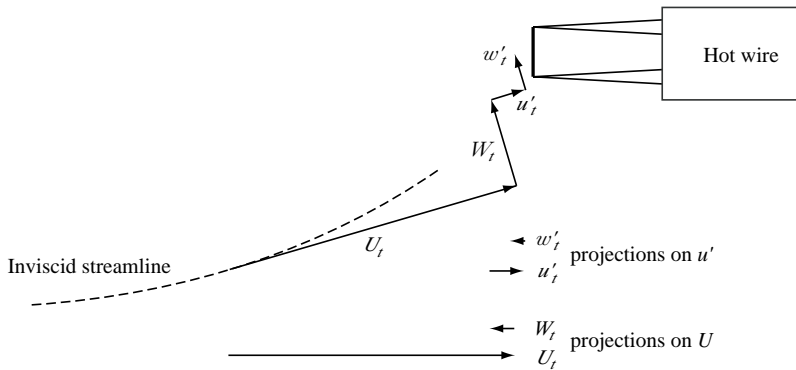FIGURE 3. Swept-wing streamline and coordinate systems.

FIGURE 4. Velocity components and hot-wire arrangement parallel to the wing surface. Note that the mean and fluctuating components of the w_t velocity are *negative* as drawn.

Stability calculations are most frequently performed using a streamline-oriented coordinate system, but physical limitations of the hot-wire traverse system require that measurements be obtained using a combination of test-section-oriented and model-oriented coordinate systems. In the test-section, or global, system, the coordinate directions are denoted X parallel to the free-stream-flow direction, Y normal to the front wall of the test section, and Z in the unswept-span direction. The global velocities are (u, v, w). The model-oriented system is defined by x perpendicular to the leading edge, y perpendicular to the chord line, and z parallel to the leading edge. Here the velocities are denoted (u_n, v_n, w_n). The various systems are shown in figure 3. The coordinate definitions are consistent with the earlier Unsteady Wind Tunnel crossflow experiments cited previously. In this experiment, hot-wire data are always acquired in the (Y, z) plane and the wire is oriented to measure the (u, v) velocity. This orientation means that velocities in the streamline-oriented coordinate system, (u_t, v_t, w_t), are measured as projections as depicted in figure 4.

The secondary-instability experiment is quite straightforward. First a stationary, spanwise-periodic primary disturbance field with an amplitude and wavelength that is uniform across the span is established, and second, the evolution of the fluctuating velocities associated with a particular stationary structure is measured. Following Reibert *et al.* (1996), periodic roughness is applied at $x/c = 0.025$, near the crossflow neutral point, to establish uniform disturbances. Because of the uniformity, only a single stationary structure need be interrogated for each case and its behaviour is

taken to be representative of the behaviour of the entire boundary layer.† Following the notation used by Reibert *et al.* (1996) and Saric *et al.* (1998), the artificial roughness arrays are designated with the notation $[k|\lambda]$, where k is the amplitude of the roughness in microns and λ is the spanwise wavelength in millimetres. During the experiment, λ is measured parallel to the leading edge, not exactly perpendicular to the crossflow-vortex axis.

Full-field streamwise-velocity scans are used for the secondary-instability measurements. These scans provide mean- and fluctuating-velocity data on a (Y, z) grid of points at a particular x/c location. Typically the spacing in Y is 200–300 µm and the spacing in z is 1.0 or 1.2 mm. This provides 15–20 points in the Y-direction from the surface to outside the boundary layer and 12–15 points in the z-direction, enough to span somewhat more than one crossflow wavelength. Full-field scans begin with a boundary-layer-profile measurement to locate the wing's surface to within several microns at the starting z position. As the scans are performed, both mean-flow and fluctuating-velocity data are obtained.

The interest here is in the process by which the instabilities grow and turbulence appears, so the fluctuations are of particular interest. At each measurement position the mean output of the hot-wire anemometer is obtained in the usual way and the fluctuating output is obtained by high-pass filtering (typically at 20 Hz) and anti-alias filtering. After filtering, the voltage output is amplified so that it covers a ± 5 V range utilizing the full range of the data-acquisition electronics.

The mean-flow data are used to determine the stationary-mode amplitude growth. This is done by considering the spanwise root mean square (r.m.s.) of the stationary disturbance, r.m.s. $[(U - U_{\mathrm{mean}})/U_{\mathrm{edge}}]$. The amplitude of the stationary-disturbance mode is represented by the integral of the mode-amplitude curve taken from the surface, $Y = 0$, to the boundary-layer edge. This measure is convenient and robust for experimental data both because it includes the contribution of all data and thus is resistant to errors at individual points and because there is no ambiguity that results from arbitrary definitions such as a point in the flow at which to evaluate the amplitude.

Power spectra of the fluctuations provide the most useful data regarding instability growth of travelling modes. To compute these spectra, the fluctuations are processed using a fast Fourier transform. A Bartlett window is employed to reduce leakage and averaging is used to reduce the variance of the power spectrum. Long samples are obtained that allow 10–20 averages to be performed while maintaining spectral resolution of about 10 Hz. The power-spectrum normalization is such that the sum of the discrete power components is equal to the sum of the discrete velocity fluctuations squared; Parseval's theorem is preserved in the discrete sense. To compute the r.m.s. amplitude of a particular frequency band, the components that lie in the band are summed, and the square root of that sum represents the r.m.s. velocity fluctuations for that band.

To obtain the instability growth rates of the travelling-wave modes, an integration over the whole field is required rather than an amplitude maximum or the amplitude at a particular location. As will be apparent below, the spatial distributions of the

---

† There is a small degree of non-uniformity across the span that results in a maximum variation of the breakdown location of approximately 5% chord. Therefore, the results presented in the following section should be interpreted as being representative of the breakdown behaviour, but they should not be taken to mean that the certain phenomena that are observed occur *precisely* at the chord locations indicated across the entire span.

modes vary through the boundary layer, so to obtain an accurate picture of the instability growth rates, the velocity-fluctuation amplitudes are integrated over the entire field to give the total mode amplitudes. Without considering changes in the spatial extent of an instability mode, much of the growth in its energy content could be lost as more of the area participates. Because the stationary distortion is so large and such strong spanwise periodicity is observed in the instability modes, simply finding the maximum or the amplitude at a certain point would not yield correct amplitude growth data. The integration of each mode is carried out over 12 mm of span, one stationary crossflow wavelength measured parallel to the leading edge. The integration in Y is carried out to the edge of the measurement region because all of the fluctuations go to zero at the top of the range.

The secondary-instability measurements presented here consist of five cases. The first of these is performed at $Re_c = 2.4 \times 10^6$ with an 18-µm-high, 12-mm-spaced roughness array at $x/c = 0.025$, $[18|12]$ roughness. This first case serves as a baseline for comparison with the other runs and is presented in the greatest detail. It will be shown that despite the new swept-wing model, this case is sufficiently similar to the behaviour observed previously to be considered a continuation of the experiments of Reibert *et al.* (1996), whose baseline was $Re_c = 2.4 \times 10^6$ with $[6|12]$ roughness. The larger roughness amplitude used here is a single layer of the smallest roughness elements that could be obtained for this experiment; the 6-µm elements used by Reibert *et al.* are no longer available. Because saturation occurs prior to breakdown, it is thought that the appearance and growth of the secondary instability may not be strongly affected by the initial amplitude.

To determine whether the secondary instability is affected by the roughness amplitude notwithstanding the saturation behaviour, a second case is performed at $Re_c = 2.4 \times 10^6$ using three layers of artificial roughness to give a $[54|12]$ array. To determine the behaviour with weakly subcritical forcing, the third case is performed with $[54|12]$ roughness at $Re_c = 2.0 \times 10^6$. Here the most amplified stationary wavelength is about 13.5 mm. Similarly, the behaviour with weakly supercritical roughness forcing is obtained from a fourth case performed with the same $[54|12]$ roughness at $Re_c = 2.8 \times 10^6$. The higher Reynolds number means that the most amplified stationary crossflow wavelength is somewhat less than 12 mm. Spanwise spectra of the mean flow for this Reynolds number indicate that the most amplified wave is about 10.2 mm. Finally, several tests are performed with enhanced free-stream acoustic and turbulent fluctuations to assess whether varying these features can have an impact on the behaviour of the secondary instability.

3. Secondary-instability results

3.1. *Baseline configuration*

The baseline configuration is $Re_c = 2.4 \times 10^6$ with $[18|12]$ roughness situated at $x/c = 0.025$. At this Reynolds number the most amplified stationary crossflow wavelength is about 12 mm (measured parallel to the leading edge), so the roughness spacing forces the most amplified wavelength. The first measurement station is at $x/c = 0.30$. This is the first position for which the quantity $\partial U/\partial Y$ equals zero somewhere inside the boundary layer, indicating that significant mean-flow distortion has developed. We first examine the boundary-layer velocity profiles spanning a single wavelength of the stationary vortex. Figure 5 shows a collection of mean-flow velocity profiles and the spanwise mean of the individual profiles. The r.m.s. curve is the stationary-disturbance mode shape. For this location, it appears that
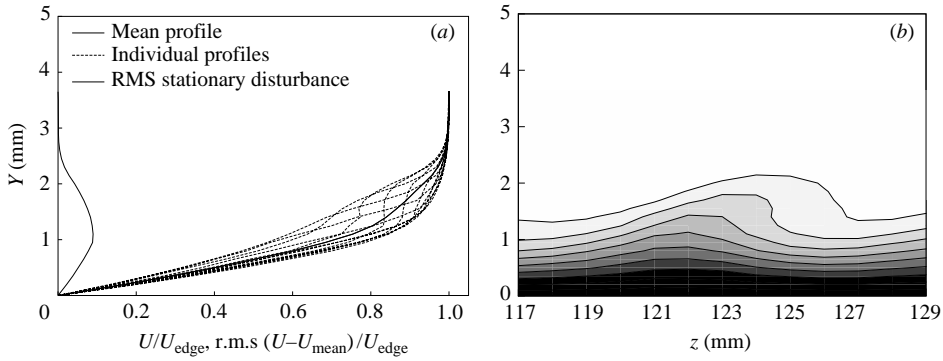
FIGURE 5. (*a*) Mean-flow velocity profiles and (*b*) contours, $Re_c = 2.4 \times 10^6$, $[18|12]$ roughness, $x/c = 0.30$, $z = 117$–128 mm. Contour lines are drawn at $U/U_{edge} = 0.10$, 0.20, ..., 0.90.
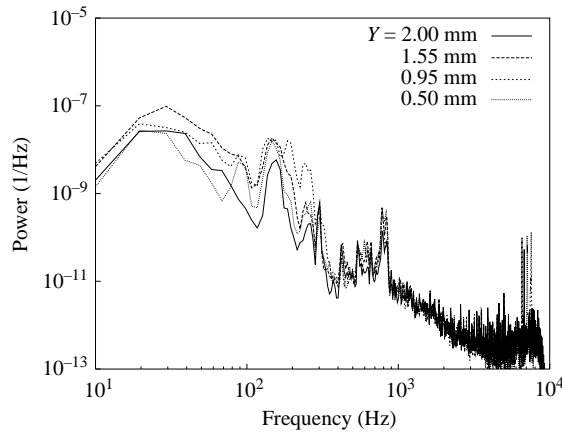

FIGURE 6. Fluctuating-velocity spectra, $Re_c = 2.4 \times 10^6$, $[18|12]$ roughness, $x/c = 0.30$, $z = 122$ mm.

although there is some distortion of the mean flow, the disturbance evolution may still be consistent with linear stability theory because the r.m.s. curve has not yet developed the upper lobe that accompanies the advent of significant nonlinearities. Reibert *et al.* (1996) explain that the development of an upper lobe is due to the rollover phenomenon that brings low-momentum fluid into the upper part of the boundary layer signalling the onset of significant mean-flow distortion, and hence, nonlinear disturbance evolution. Figure 5 also includes contours of streamwise mean velocities. In this plot the streamwise flow is into the page and the crossflow velocity is from right to left. Viewed from this orientation, the stationary vortex rotates in the clockwise sense. The dark shades are low-momentum regions and the light shades are high-momentum regions.

The spatial and spectral distributions of velocity fluctuations within the stationary structure are particularly important for understanding the breakdown of the boundary layer. Figure 6 shows the velocity-fluctuation spectra at several points on a wall-normal (constant-*z*) line. Although the spectra at this location are low amplitude, several features are detected. First, the high-amplitude disturbances between 150 and 200 Hz are the most amplified travelling crossflow waves. Second, there are fluctuations near 800 Hz. These fluctuations are most prominent in the region
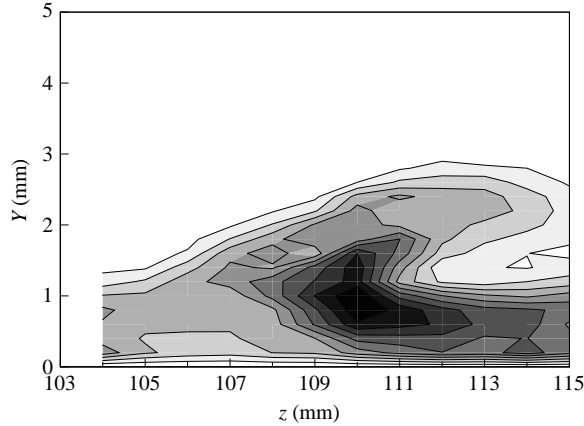
FIGURE 7. 200 Hz velocity-fluctuation r.m.s. distribution, $Re_c = 2.4 \times 10^6$, $[18|12]$ roughness, $x/c = 0.35$, 200 Hz (i.e. 100–300 Hz) bandpass. Lines are 10% contours of the maximum in this band.

of strongly decelerated wall-normal velocity profiles and correspond to a non-dimensional frequency $F = 2\pi f v / U_\infty^2 \times 10^6 = 140$. Both of these factors suggest that the 800 Hz fluctuations, although localized, may be related to a streamwise instability similar to T–S waves. Third, the lowest frequencies near 30 Hz are associated with unavoidable low-level background fluctuations of the wind tunnel. The amplitude fall off below 10 Hz is due to the high-pass filter applied as part of the hot-wire signal conditioning. Although the power density (signal power per Hz) at these frequencies is high, it should be noted that as a band, the low frequencies contain relatively little power because the band quite is narrow.

Moving to $x/c = 0.35$, the earliest stage of nonlinear evolution is apparent in the mean flow; a contour plot obtained here would show that overturning of the low-momentum upwelling is well under way. The spectra are quite similar to what is observed upstream, but at this location there is significantly more variation across the span. Figure 7 shows that the 200 Hz travelling-wave fluctuations are strongly modulated due to an interaction with the stationary disturbance. In fact, it may not be appropriate to refer to these fluctuations as travelling crossflow waves once the modulation becomes so severe. Fischer & Dallmann (1991) predicted this effect using Floquet theory and referred to it as a secondary instability. Malik, Li & Chang (1994) also predicted this effect using an NPSE approach and argued that the modulation is simply a result of the nonlinear interaction of the stationary and travelling disturbances that becomes more pronounced as the disturbance amplitudes increase. The experimental evidence supports the notion of a continuous progression from the original, spanwise-uniform state to the state seen in figure 7, and therefore, this effect is better described as a modulation of the primary travelling disturbance modes than as a secondary instability.

It is not obvious that this experiment should be capable of detecting these fluctuations as distinctly as they are observed here. The primary disturbance consists of streamwise vorticity or v', w' velocities and the hot wire is situated to detect u', v' fluctuations. Furthermore, because the streamwise U component is large relative to the fluctuations, the hot wire is more capable of detecting the u' fluctuations than the v' fluctuations that simply change the velocity vector's direction but do not significantly change its amplitude. The fluctuating velocity detected by the hot wire
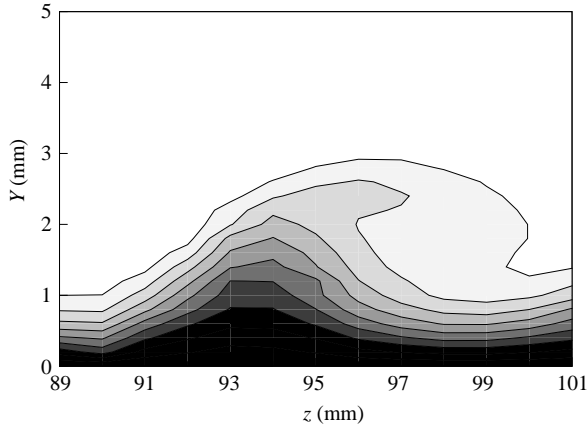
FIGURE 8. Mean-flow velocity contours, $Re_c = 2.4 \times 10^6$, $[18|12]$ roughness, $x/c = 0.40$, contour lines at $U/U_{\text{edge}} = 0.10, \ 0.20, \ \ldots, \ 0.90$.
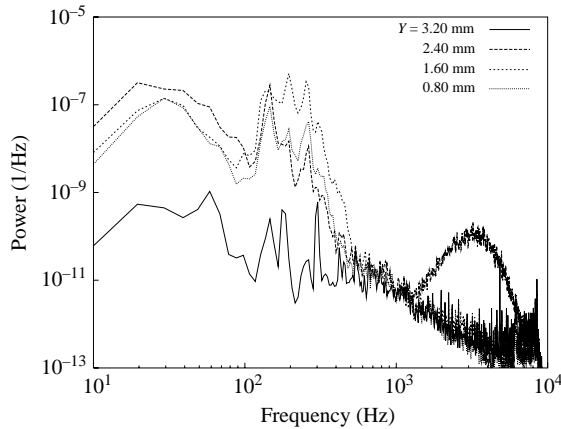

FIGURE 9. Fluctuating-velocity spectra, $Re_c = 2.4 \times 10^6$, $[18|12]$ roughness, $x/c = 0.40$, $z = 94$ mm.

is $[(U + u')^2 + v'^2]^{1/2} - U$, which is approximately equal to u' for $u', v' \ll U$. What this analysis does not consider, however, is the fact that the inviscid streamlines and crossflow vortices are inclined relative to the X-axis. This means that the hot wire actually detects a component of the w' fluctuations that appears with mean velocity, U, in the simple analysis presented above. This arrangement is shown schematically in figure 4.

At $x/c = 0.40$, the stationary-mode amplitude is substantially increased (figure 8). Here, spectra at multiple span locations show evidence of a high-frequency mode. Spectra from the centre of the upwelling region (figure 9) show that a broad band of fluctuations extends from 1 kHz to 5 kHz, with a maximum amplitude somewhat above 3 kHz. At all span stations, the 200 Hz fluctuations are also strongly amplified.

The spatial distribution of the 3.0 kHz fluctuations (figure 10) shows that these fluctuations lie along the shear layer to the left of the upwelling region and extend over much of the span of the stationary structure. The high frequencies represent a secondary instability in the strictest sense because neither the high-frequency band nor
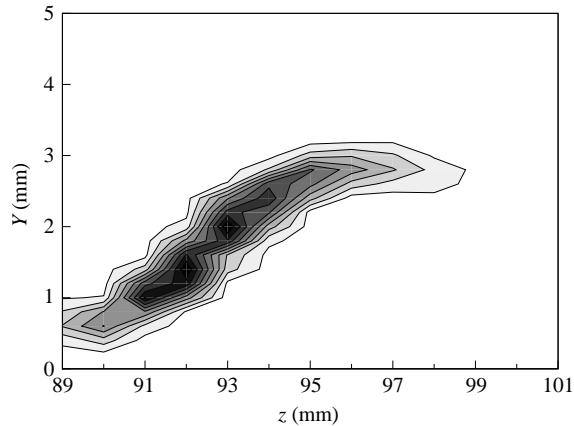
FIGURE 10. 3.0 kHz velocity-fluctuation r.m.s. distribution, $Re_c = 2.4 \times 10^6$, $[18|12]$ roughness, $x/c = 0.40$, 200 Hz bandpass. Lines are 10% contours of the maximum in this band.

the spatial location at which the fluctuations exist are associated with an instability of the undistorted mean flow. The location at which the 3.0 kHz fluctuations occur is not what was reported by Kohama *et al.* (1991) but instead agrees with the computations of Malik *et al.* (1999) and Koch *et al.* (2000) and with measurements on swept plates by Lerche (1996) and Kawakami *et al.* (1999). The location of the 3.0 kHz mode relative to the mean-flow distribution indicates that its production is probably dominated by the spanwise gradient of the streamwise velocity, $\partial U / \partial z$. This is what Malik *et al.* (1996) termed a mode-I secondary instability. The shape and extent of this mode reinforce the need for full-field as opposed to single-line scans to adequately understand the secondary instability. Obviously, the choice of wall offset, Y, for a single-line scan is very important for the relationship of the mode-I amplitude distribution to the underlying mean flow.

   Because the secondary instability is situated where it is, aligned on the high-velocity shear layer along the left edge of the low-momentum upwelling, it appears that this is an inviscid, inflection-point-driven instability. As such it is manifested as vortex lines that lie in the (Y, z)-plane and convect in the stream direction. Therefore, a visualization of the secondary instability would consist of rolls that wrap along the left side of and extend above the stationary structure. This is exactly what is observed in flow-visualization experiments of rotating-disk boundary layers by Kohama (1984, 1985), in a swept-plate boundary layer by Kohama & Egami (1999), and in the recent direct numerical simulation (DNS) studies by Wassermann & Kloker (2002).

   The distribution of 200 Hz fluctuations continues to diverge from what is predicted for travelling crossflow waves by linear theory. At $x/c = 0.40$, there is almost no significant activity in this band in the high-velocity regions that are being drawn into the surface by the stationary vortex, and the fluctuations that were once distributed along the surface as the travelling crossflow waves are lifted by the vortex in the low-momentum upwelling region. The behaviour of this mode is certainly worthy of much more detailed attention. However, to do it justice would require a different technique than is used here. Because it is (or at least starts as) a v', w' disturbance, if one wishes to understand its evolution unambiguously, a multi-element hot-wire probe should be used to obtain the projection of the velocity field onto the plane parallel to the surface instead of simply the projection onto the single-element wire used here. With the data that are available now, nothing more conclusive can be said about this
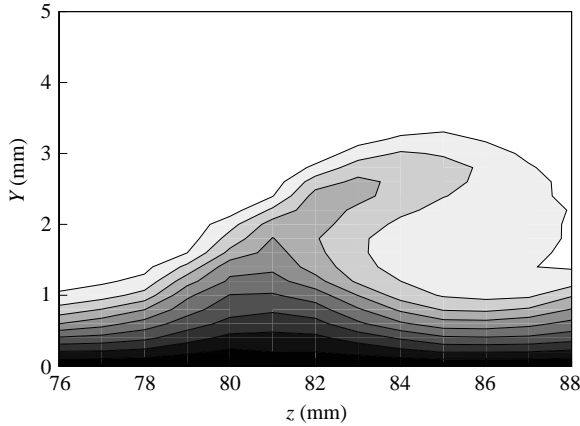
FIGURE 11. Mean-flow velocity contours, $Re_c = 2.4 \times 10^6$, $[18|12]$ roughness, $x/c = 0.44$, contour lines at $U/U_{\text{edge}} = 0.10, \ 0.20, \ \ldots, \ 0.90$.
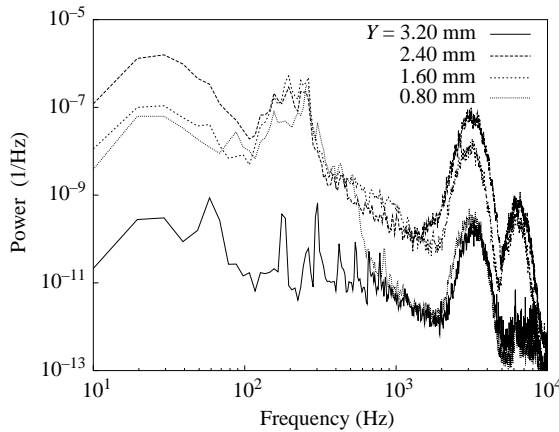

FIGURE 12. Fluctuating-velocity spectra, $Re_c = 2.4 \times 10^6$, $[18|12]$ roughness, $x/c = 0.44$, $z = 81$ mm.

mode. This does not prevent us from moving forward with the high-frequency mode. Because this mode lies along a streamwise shear layer, the disturbances are u', w' (or u', v', depending on the particular location being considered) and a single hot wire is sufficient to obtain good data.

At $x/c = 0.44$, the mean-flow behaviour remains the same as before (see figure 11). The fluctuation spectra show large secondary instability amplitudes both at the mode-I frequency, 3.0 kHz, and now for the first time at a higher frequency, 6.1 kHz. To the left of the upwelling region, the spectra show only a hint of this higher-frequency mode. However, at $z = 81$ mm, the centre of the upwelling region (figure 12), the amplitude of the new 6.1 kHz mode is quite dramatic. In the overturning region, the spectra obtained at $z = 84$ mm do not show evidence of the highest frequency mode and show relatively low amplitudes for the 3.0 kHz mode. It is interesting to note that the overturning location, $z = 84$ mm, is exactly the location at which a secondary instability might be expected based solely on the $U(Y)$ profiles. These profiles include multiple inflection points in regions of high shear stress and high velocity at the top of the vortex structure. However, at this location there is almost no secondary-instability
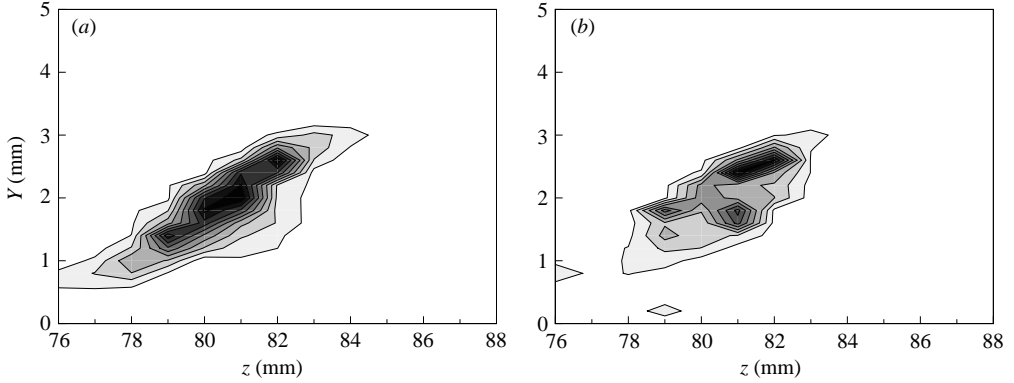
FIGURE 13. (*a*) 3.0 kHz and (*b*) 6.1 kHz velocity-fluctuation r.m.s. distribution, $Re_c = 2.4 \times 10^6$, $[18|12]$ roughness, $x/c = 0.44$, 200 Hz bandpass. Lines are 10% contours of the maximum in each band.
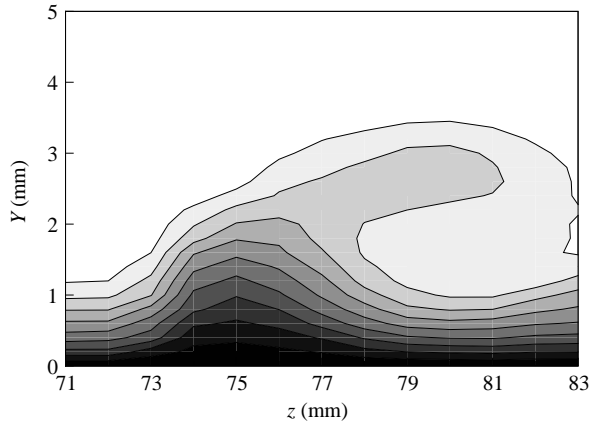

FIGURE 14. Mean-flow velocity contours, $Re_c = 2.4 \times 10^6$, $[18|12]$ roughness, $x/c = 0.46$, contour lines at $U/U_{\text{edge}} = 0.10, \ 0.20, \ \ldots, \ 0.90$.

activity. The spatial distributions of the 3.0 kHz and 6.1 kHz modes are given in figure 13. These plots show that the two modes are spatially coincident, so it is only because of their frequency separation that they can be recognized as distinct modes.

The situation at $x/c = 0.45$ is quite similar to that at $x/c = 0.44$. The fluctuation spectra show that the 3.0 kHz and 6.1 kHz modes continue to grow rapidly, now with points at nearly half the span locations participating. The spatial distribution of the 6.1 kHz peak has matured significantly beyond $x/c = 0.44$; it now lies clearly along the shear layer to the left of the low-momentum upwelling zone coincident with the location of the 3.0 kHz activity shown previously, whereas before it was a somewhat ambiguous blob (see figure 13). Despite the fact that the 6.1 kHz mode is located at the same position as the 3.0 kHz mode and is at almost twice its frequency, a comparison of the modes' growth rates given below indicates that the 6.1 kHz mode is not a harmonic of the 3.0 kHz mode.

Finally, at $x/c = 0.46$, localized breakdown occurs. Figure 14 shows that much of the fine structure of the mean flow has been eliminated. The low-momentum upwelling no longer has a narrow apex; instead this region is wider and flatter. The
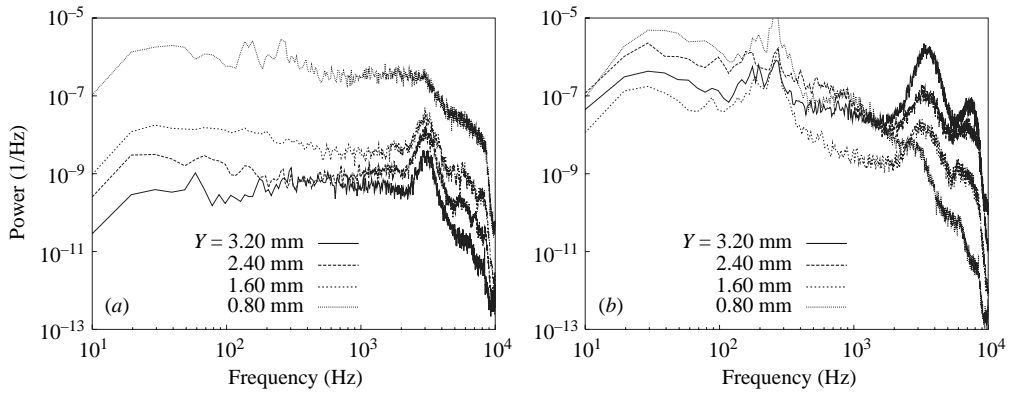
FIGURE 15. Fluctuating-velocity spectra, $Re_c = 2.4 \times 10^6$, $[18|12]$ roughness, $x/c = 0.46$, (a) $z = 72$ mm and (b) $z = 78$ mm.

region of low-momentum fluid high in the boundary layer still extends over nearly the whole stationary structure's length, but now the lowest velocities in this feature, $U < 0.7U_{edge}$, are gone. What is most important in figure 14, however, is the velocity gradient near the wall to the left of the low-momentum upwelling. This region looks quite different from previous cases; in particular the contour lines are now very close together, indicating that the wall shear here is quite high.

What are responsible for these changes in the mean flow are of course the much-increased velocity fluctuations brought on by breakdown to turbulence. Figure 15 shows fluctuation spectra at $z = 72$ mm, the high-wall-shear region to the left of the low-momentum upwelling zone and at $z = 78$ mm. The spectra at $z = 72$ mm include a flat, very high-amplitude, turbulent spectrum at $Y = 0.8$ mm, the position in the figure closest to the wall. The spectra higher in the boundary layer are similar, but in these curves some evidence of the 3.0 kHz mode remains. The situation is much the same for $z = 75$ mm, the centre of low-momentum upwelling, except that the spectrum of the point closest to the wall shows a somewhat lower fluctuation level, especially beyond 2 kHz. This position is below the zone affected by the secondary instabilities at the upstream stations and below the travelling-crossflow fluctuations that exist throughout the preceding development, just as they appeared in figure 7. The spectra for $z = 78$ mm that are shown in figure 15 are not turbulent; they maintain distinct spectral features associated with travelling-crossflow fluctuations near 200 Hz and the 3.0 kHz mode-I secondary instability despite their high amplitude.

In figure 16 the total velocity-fluctuation r.m.s. distribution is plotted. It is evident from this figure that the overall energy distribution is spatially coincident with the 3.0 kHz and 6.1 kHz modes. The rapid growth of these modes just prior to breakdown and the spatial location of the subsequent fluctuation maximum make it quite obvious that the secondary instability is the route to breakdown for this flow. Notice that this distribution shows somewhat more activity close to the wall between $z = 71$ and 73 mm than do the 3.0 kHz distributions upstream. This has an important consequence in that it helps to explain the high wall shear in this region; the turbulent fluctuations promote enhanced mixing of the high-momentum fluid with the low-momentum fluid near the wall, resulting in increased shear. As a result, the behaviour of the turbulent wedges that indicate breakdown in naphthalene flow-visualization experiments of Dagenhart & Saric (1999) is now clear. The upstream tips of the wedges appear at the points where the mode-I instability makes its closest approach to the wall on
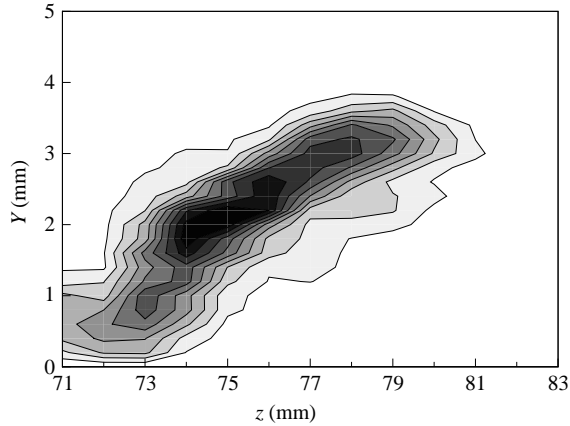
FIGURE 16. Total velocity-fluctuation r.m.s. distribution, $Re_c = 2.4 \times 10^6$, $[18|12]$ roughness, $x/c = 0.46$, 20 Hz–8.0 kHz bandpass. Lines are 10% contours of the maximum r.m.s. fluctuations.

the left side of the low-momentum upwelling location. Understanding the location and amplitude of boundary-layer features relative to the associated wall shear in this manner is essential if one is to conduct an experiment using only wall measurements with hot films or some other technique as would be required in a flight experiment. In particular, consider the quantitative transition-detection technique developed by Chapman *et al.* (1998) using hot films. In this approach, the hot films are aligned in an array along a particular stationary structure and must be positioned within the structure to detect the secondary-instability fluctuations and the high shear of the turbulent wedge. With the data presented here, it is now possible to correctly place the sensors to achieve optimum performance with this technique.

It is not clear why these high-amplitude fluctuations appear as close to the surface as they do just aft of breakdown. Comparing figure 16 to the upstream 3.0 kHz and 6.1 kHz distributions shows that while the maxima are located in the same region of the stationary structure, the total fluctuation contours come much closer to the surface than the individual mode contours that we have been tracking. One possibility is that the small counter-rotating stationary vortex predicted by the computations of Malik *et al.* (1994) and the DNS study of Wintergerste & Kleiser (1996) is of sufficiently high amplitude to either participate in breakdown or transport fluctuation energy closer to the wall in this region. This mechanism is not directly supported by the present data and Wassermann & Kloker (2002) find that the vortex is quite weak, so this possibility requires more investigation.

Downstream of the breakdown location we expect the stationary structure to dissolve quickly in the face of the enhanced fluctuation levels. This is evident at $x/c = 0.47$ in the mean-flow velocity contours of figure 17. This figure shows the continuing breakup of the low-momentum zone high in the boundary layer and the extension of the high-wall-shear zone. These trends continue at $x/c = 0.48$, the last measurement station of the baseline case. For that final location, spectra 3 mm to the left of, centred on, and 3 mm to the right of the low-momentum upwelling region are all nearly fully turbulent, with amplitudes decreasing away from the wall. Spectra obtained 6 mm to the right of the low-momentum upwelling centre (half the stationary-mode wavelength) still exhibit relatively low fluctuation levels as this location has still not been contaminated by the spreading turbulent wedge.
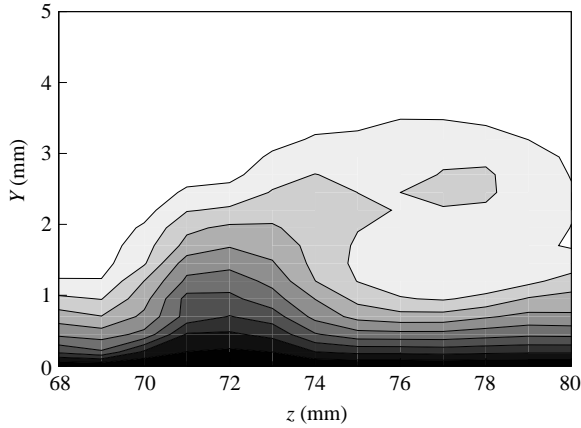
FIGURE 17. Mean-flow velocity contours, $Re_c = 2.4 \times 10^6$, $[18|12]$ roughness, $x/c = 0.47$, contour lines at $U/U_{\text{edge}} = 0.10, \ 0.20, \ \ldots, \ 0.90$.
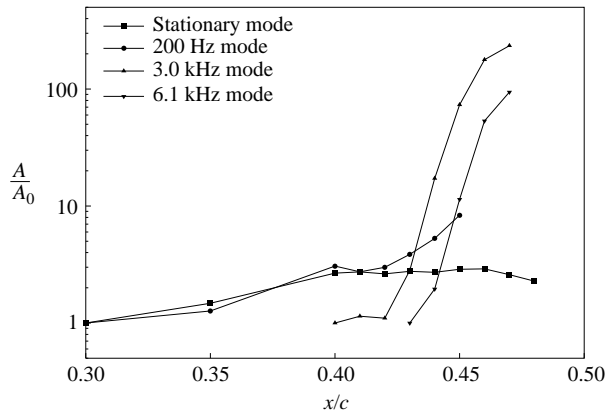

FIGURE 18. Velocity-fluctuation r.m.s. growth, $Re_c = 2.4 \times 10^6$, $[18|12]$ roughness.

The growth of each mode is shown in figure 18. Each curve is normalized using the amplitude at which it is first observed. The figure shows that the stationary disturbance grows between $x/c = 0.30$ and $x/c = 0.40$, but that downstream of $x/c = 0.40$, the stationary disturbance is saturated. The saturation amplitude is 19% based on the peak of the stationary r.m.s. curve. Throughout the chord range, the travelling-crossflow amplitude grows slowly. Its development past $x/c = 0.45$ is not plotted because once the flow becomes turbulent, the spectral band that defines this mode, 100–300 Hz, contains significant fluctuation levels that are clearly not associated with the same mode. The most important and dramatic features of this plot are the 3.0 kHz and 6.1 kHz mode curves. These appear in quick succession at $x/c = 0.40$ and $x/c = 0.43$, respectively. The 3.0 kHz mode does not amplify rapidly at first, but starting at $x/c = 0.42$, it undergoes very rapid exponential growth until breakdown at $x/c = 0.46$. It is rather curious that the 3.0 kHz mode exists for 2% chord before undergoing rapid growth. One might think from this behaviour that the 2.9–3.1 kHz band includes two distinct modes: a weaker early mode and the strongly amplified mode that becomes unstable at $x/c = 0.42$. This may indeed be the case, but if so, it would be difficult or impossible to detect experimentally because the 3.0 kHz
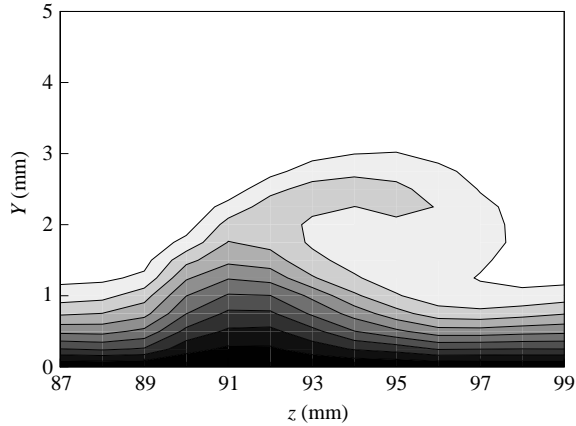
FIGURE 19. Mean-flow velocity contours, $Re_c = 2.4 \times 10^6$, $[54|12]$ roughness, $x/c = 0.38$, contour lines at $U/U_{edge} = 0.10,\ 0.20,\ \ldots,\ 0.90$.

fluctuations are always observed at exactly the same (Y, z) location, regardless of the chord location. The 6.1 kHz mode is first detected at $x/c = 0.43$ and it undergoes somewhat stronger growth than the 3.0 kHz mode. As mentioned above, the growth rate of the 6.1 kHz mode is not twice that of the 3.0 kHz mode, meaning that the 6.1 kHz mode is not simply a harmonic of the 3.0 kHz mode, despite the fact that they are spatially coincident. Rather, it appears that the 3.0 kHz and 6.1 kHz modes are distinct.

3.2. High-amplitude-roughness configuration

With a fairly complete description of the secondary instability for the baseline case of $Re_c = 2.4 \times 10^6$ with $[18|12]$ roughness, we wish to understand the effect of roughness amplitude on the secondary instability. To accomplish this we use a new configuration that retains $Re_c = 2.4 \times 10^6$ but features $[54|12]$ roughness. The results of Reibert *et al.* (1996) show that if the stationary crossflow waves saturate (as they do here), then the transition location is nearly independent of the roughness amplitude. The implication for this work is that because the stationary crossflow disturbances are saturated at 19% amplitude by $x/c = 0.40$ in the baseline configuration, increasing the roughness amplitude will change neither the saturated stationary-mode amplitude nor the transition location. Furthermore, one might expect that if these features are unchanged, the behaviour of the secondary instability will be unchanged as well.

The stationary boundary-layer structure that is tracked for this case saturates farther upstream than the structure in the baseline case, so the measurements begin at $x/c = 0.25$. At $x/c = 0.34$, the first indication of type-I secondary-instability activity is observed near 3.0 kHz. By $x/c = 0.37$, there is evidence of 6.1 kHz activity. By $x/c = 0.38$, this has grown to the extent that it can be extracted into a distinct mode shape. The mean flow at $x/c = 0.38$ is shown in figure 19 and representative spectra from $z = 91$ mm are shown in figure 20. What is striking about these spectra is that the low-frequency fluctuations appear to be much more important in this case than in the baseline configuration. The peak of the low-frequency spectrum is not of significantly higher amplitude than what was observed before, but the amplified band extends to significantly higher frequencies than were observed in the baseline case. The distribution of 200 Hz fluctuations given in figure 21(*a*) is similar to what is
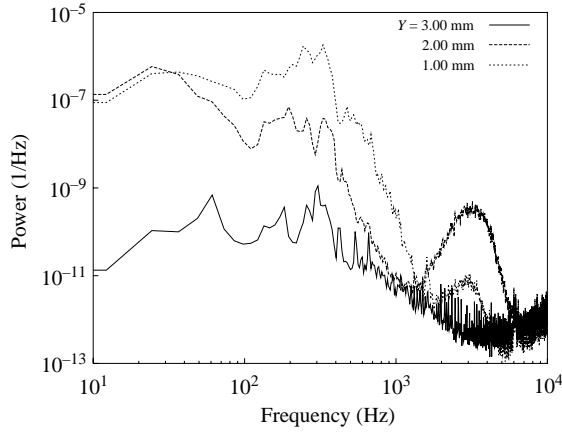
FIGURE 20. Fluctuating-velocity spectra, $Re_c = 2.4 \times 10^6$, $[54|12]$ roughness, $x/c = 0.38$, $z = 91$ mm.
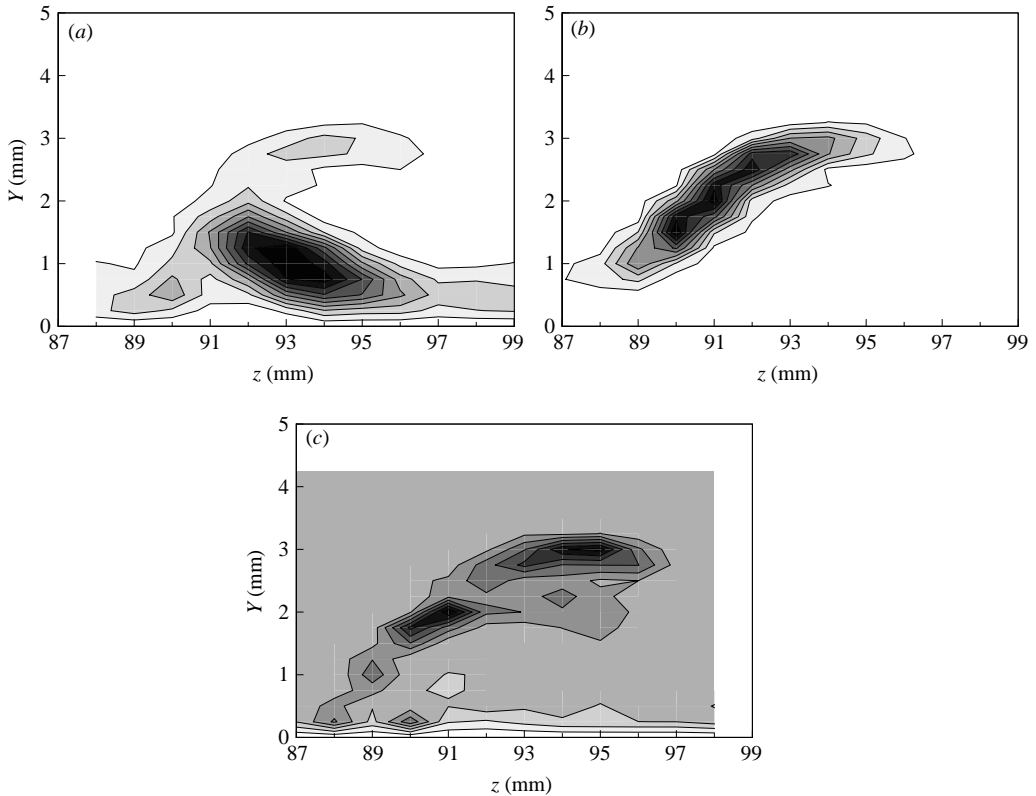

FIGURE 21. (*a*) 200-Hz, (*b*) 3.0-kHz, (*c*) 6.1-kHz velocity-fluctuation r.m.s. distribution, $Re_c = 2.4 \times 10^6$, $[54|12]$ roughness, $x/c = 0.38$, 200-Hz bandpass. Lines are 10% contours of the maximum in each band.

observed with $[18|12]$ roughness, but here there is the additional feature of a local amplitude maximum to the left of the low-momentum upwelling location, situated close to the surface at $Y = 0.5$ mm.

The 3.0 kHz distribution at $x/c = 0.38$ (figure 21*a*) is about the same as those shown previously. The 6.1 kHz distribution (figure 21*c*), however, is quite different from what is observed in the baseline experiment. Here, the peak amplitude is not located at the same point on the high-velocity shear layer as the 3.0 kHz mode. Instead, the highest amplitude 6.1 kHz fluctuations are on the top of the overturning region, the location with strong $\partial U/\partial Y$ gradients. This mode is different from what is observed for $[18|12]$ roughness and instead appears to be what Malik *et al.* (1996) term a type-II secondary instability. It is also an inflectional instability, but now the energy production is dominated by the $\partial U/\partial Y$ gradient and the u', v' fluctuation terms, whereas the type-I instability is driven primarily by the $\partial U/\partial z$ gradient and the u', w' fluctuations. Figure 21 shows that there is 6.1 kHz activity in that part of the structure where the 3.0 kHz activity is greatest, so there may be two separate modes at 6.1 kHz that are simultaneously active.

The appearance of a type-I mode upstream of where a type-II mode is observed is somewhat surprising in the light of computational results. Malik *et al.* (1999) find that for the swept-wing geometry and disturbance amplitudes of Reibert *et al.* (1996) (both of which are very similar to the present experiments) the most amplified type-II mode has a higher growth rate than the most amplified type-I mode just downstream of where both are destabilized. Only farther downstream does the type-I mode's growth rate equal that of the type-II mode. Other experiments observe that higher-frequency disturbances appear downstream of lower-frequency disturbances (e.g. figure 11 from Kawakami *et al.* 1999), but this offers only partial confirmation of the present result as it is unclear whether the higher frequencies observed previously correspond to type-I or type-II modes. The origin of this apparent discrepancy may be the initial amplitudes of the various secondary instability modes. If type-I modes have significantly higher initial amplitudes than the type-II modes they could easily be observed first in spite of their lower growth rates. While nothing is known about the receptivity of the secondary instabilities, the fact that the amplitude of the background turbulence decreases with frequency suggests that the lower-frequency type-I modes are likely to have larger initial amplitudes.

At $x/c = 0.39$, the mean-flow contours are essentially unchanged and the secondary instability modes retain their earlier character. The 6.1 kHz type-II mode is still not of high enough amplitude to render the background fluctuation level unimportant, so an energy integral would include a large contribution from the region outside the mode. This is one drawback of the whole-field integration technique; it cannot be used to pinpoint very low-amplitude modes. Moreover, the type-II mode continues to droop into the mode-I region, so it is impossible to determine whether the measurements are detecting a single mode or two separate mechanisms that overlap both spatially and spectrally.

At $x/c = 0.40$, breakdown occurs. The contours in figure 22 indicate that the mean flow has already lost much of its structure high in the boundary layer and that the wall shear has increased dramatically. The velocity-fluctuation spectra are not as dramatic as the turbulent spectra that indicated breakdown for the baseline $[18|12]$ case, but there is a considerable loss of spectral structure. In particular, the mode-I and mode-II secondary instabilities decrease in amplitude from $x/c = 0.39$ to $x/c = 0.40$. Lacking a more clear indication, the combination of the mean flow and spectral changes is taken as the breakdown criterion in this case. The most interesting feature of this case is that following breakdown, the total r.m.s. velocity fluctuations (shown in figure 23) are coincident with the location of 200 Hz activity and not with either of the secondary-instability modes. Despite this, the increase in wall shear occurs across
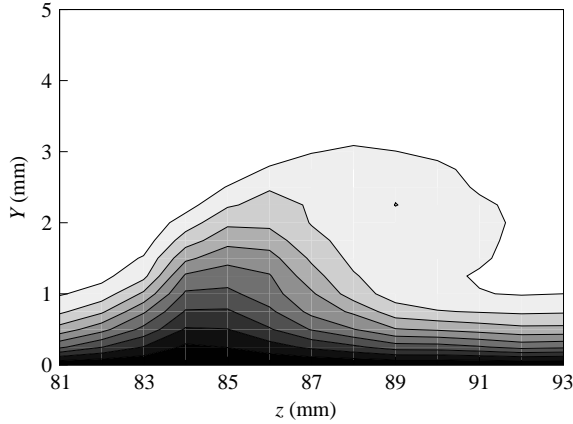
FIGURE 22. Mean-flow velocity contours, $Re_c = 2.4 \times 10^6$, $[54|12]$ roughness, $x/c = 0.40$, contour lines at $U/U_{\text{edge}} = 0.10, 0.20, \ldots, 0.90$.
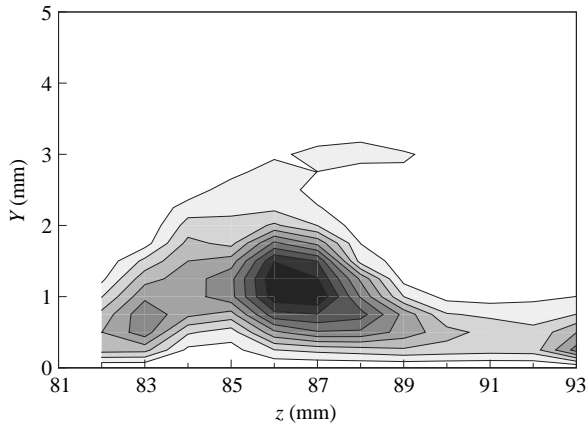

FIGURE 23. Total velocity-fluctuation r.m.s. distribution, $Re_c = 2.4 \times 10^6$, $[54|12]$ roughness, $x/c = 0.40$, 20 Hz–8.0 kHz bandpass. Lines are 10% contours of the maximum r.m.s. fluctuations.

the entire spanwise extent of the structure, including the region to the left of the upwelling region that is more closely associated with the secondary than the primary fluctuations.

The growth rates of the stationary crossflow vortex, the 200 Hz mode, and the 3.0 kHz mode are shown in figure 24. The 6.1 kHz mode is not shown both because it never appears as a distinct mode and because its amplitude is so low that an amplitude integration would include a significant contamination by the background. The 200 Hz mode grows throughout the entire boundary layer with a growth rate that does not change nearly as much as one might expect given the dramatic variations that occur in the underlying mean flow. The 3.0 kHz mode-I instability has a lower growth rate here than was observed in the baseline case. It is not known whether this is a consequence of the growth being observed upstream of that in the baseline case or is a purely local effect that only depends on the details of the stationary structure. The most significant observation here is that the growth and amplitude of the low-frequency fluctuations cannot be ignored relative to the high-frequency
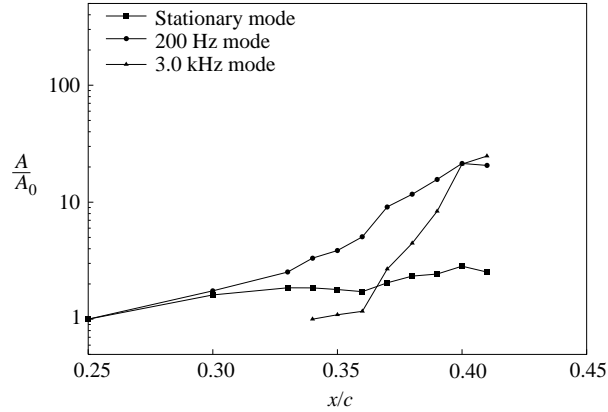
FIGURE 24. Velocity-fluctuation r.m.s. growth, $Re_c = 2.4 \times 10^6$, $[54|12]$ roughness.

fluctuations. In this case, both types of fluctuations may be jointly responsible for breakdown.

The stationary-mode growth curve displays a notched appearance, that is, growth and saturation followed by a slight decrease in amplitude, then slightly more growth before breakdown. Although it is more obvious here, the same phenomenon occurs in the baseline case (figure 18). This behaviour was observed by Reibert *et al.* (1996) using $[18|12]$ and $[48|12]$ but not $[6|12]$ roughness. Those experimental results were duplicated by the NPSE results of Malik *et al.* (1999) and Haynes & Reed (2000) and, therefore, this appears to be a real effect and not experimental error. Although the mechanism is not clear, these variations might be the long-wavelength steady oscillations of the nonlinear equilibrium solutions found by Koch *et al.* (2000).

3.3. *Reduced-Reynolds-number configuration*

We now move to $[54|12]$ roughness with $Re_c = 2.0 \times 10^6$. This configuration demonstrates the effect slightly subcritical forcing has on the secondary instability and breakdown; the lower Reynolds number means that the most amplified stationary wavelength is longer than 12 mm, about 13.5 mm. The lower Reynolds number will produce transition at a larger value of x/c, but what is of primary interest is the identification of the secondary-instability modes and the relative importance of the secondary modes to the fluctuations of the primary instability.

The measurements for this case begin at $x/c = 0.40$, where there is already some overturning of the stationary structure but the fluctuation spectra are all of very low amplitude. The structure develops with only the low-frequency mode detected until $x/c = 0.46$, where a type-I secondary mode first appears, centred at 2.4 kHz. A 200 Hz low-frequency mode demonstrates the same sort of redistribution that was observed for the preceding cases. At $x/c = 0.50$, the mean-flow contours and spectra show that for this Reynolds number and roughness configuration, the boundary layer has more of the character of the baseline case than of the high-amplitude-roughness configuration. The low-frequency mode does not extend to higher frequencies and the mode-I secondary-instability frequency is growing significantly.

Moving to $x/c = 0.55$, the appearance of the instability modes is quite dramatic. The mean-flow contours (figure 25) are similar to the preceding cases, but now the spectra (figure 26) show dramatic growth of the mode-I peak as well as at least two additional modes at two and three times the frequency of the mode-I peak. The spatial
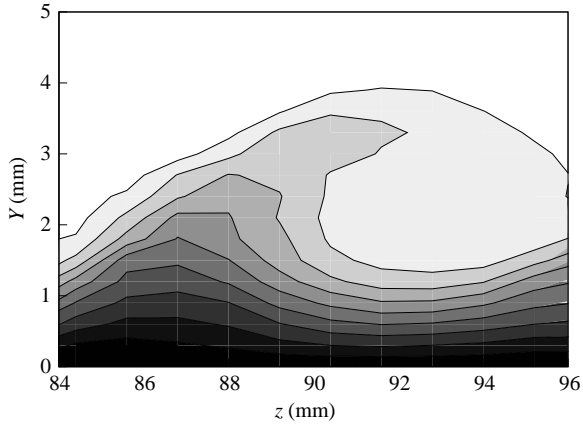
FIGURE 25. Mean-flow velocity contours, $Re_c = 2.0 \times 10^6$, $[54|12]$ roughness, $x/c = 0.55$, contour lines at $U/U_{\text{edge}} = 0.10, \ 0.20, \ \ldots, \ 0.90$.
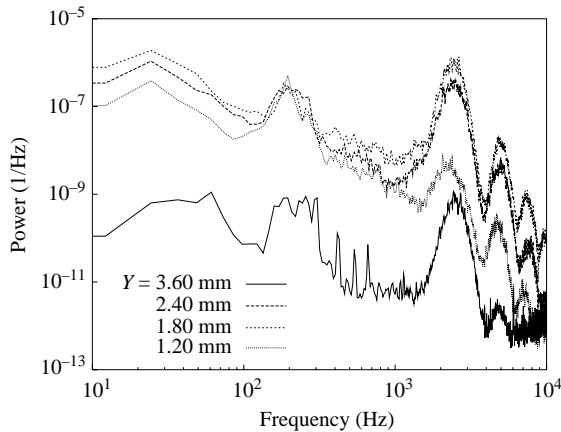

FIGURE 26. Fluctuating-velocity spectra, $Re_c = 2.0 \times 10^6$, $[54|12]$ roughness, $x/c = 0.55$, $z = 85.6$ mm.

distributions of the 2.4 kHz, 4.9 kHz, and 7.5 kHz modes are shown in figure 27. (The 200 Hz mode appears in its usual position relative to the mean-flow structure.) At this chord location, all of the high-frequency modes lie in the mode-I orientation where the $\partial U/\partial z$ shear is strongest. There is no evidence of mode-II behaviour.

Breakdown is first detected at $x/c = 0.57$. The mean-flow distribution is essentially unchanged, but the spectra near the wall to the left of the low-momentum upwelling region have a flat, turbulent character. Once again, breakdown is highly localized, because spectra obtained elsewhere in the field do not show evidence of turbulence. The total velocity-fluctuation r.m.s. distribution is shown in figure 28. This figure shows that the low- and high-frequency activity are about equally important for this breakdown scenario because the two regions of the stationary structure have equal intensities. The growth of the r.m.s. fluctuations (figure 29) in this case is quite similar to what is observed in the baseline case. Two distinct type-I secondary-instability modes centred at 2.4 kHz and 4.9 kHz can be tracked for many chord stations. Unlike the baseline case, the 4.9 kHz mode does appear to be a true harmonic of the 2.4 kHz mode. At no position in the transition region are type-II modes detected.
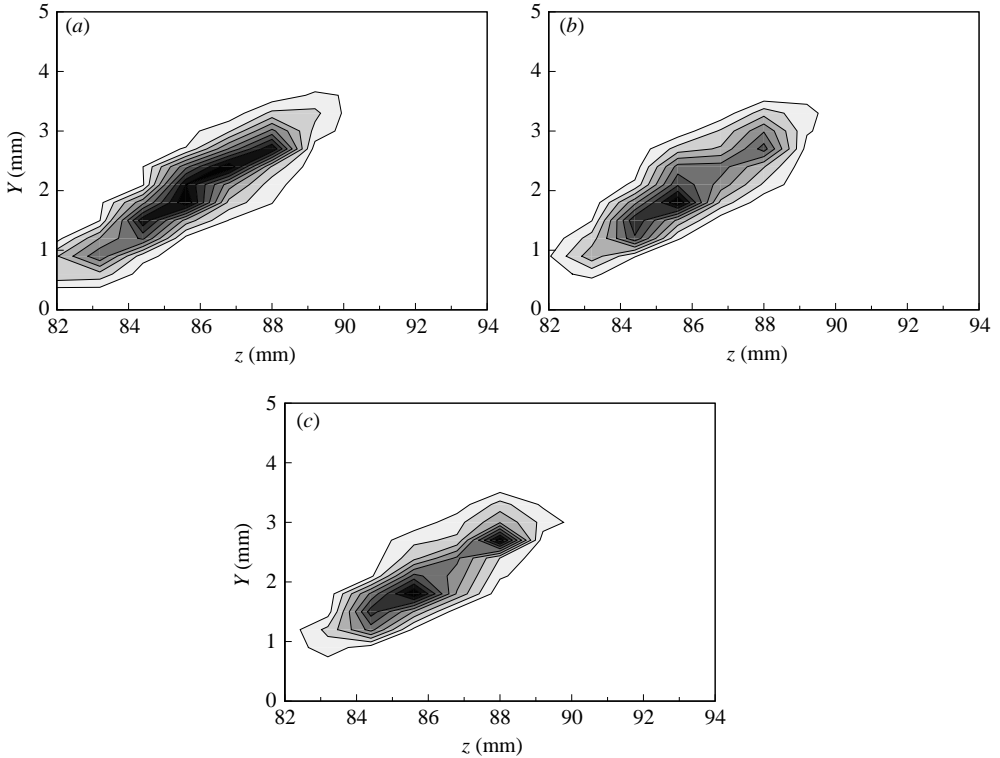
FIGURE 27. (*a*) 2.4 kHz, (*b*) 4.9 kHz, and (*c*) 7.5 kHz velocity-fluctuation r.m.s. distribution, $Re_c = 2.0 \times 10^6$, $[54|12]$ roughness, $x/c = 0.55$, 200 Hz bandpass. Lines are 10% contours of the maximum in each band.
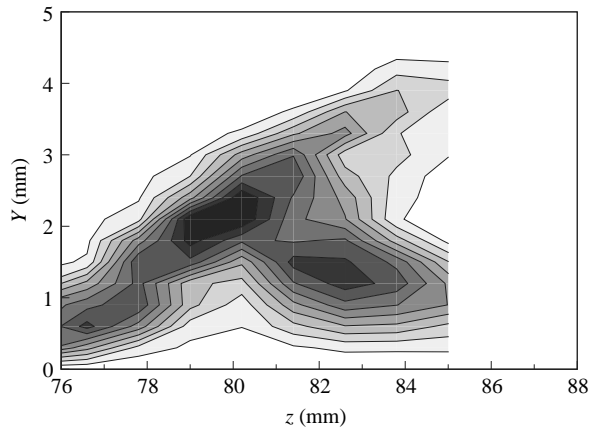

FIGURE 28. Total velocity-fluctuation r.m.s. distribution, $Re_c = 2.0 \times 10^6$, $[54|12]$ roughness, $x/c = 0.57$, 20 Hz–12.0 kHz bandpass. Lines are 10% contours of the maximum r.m.s. fluctuations.

3.4. *Increased-Reynolds-number configuration*

As a fourth case we consider $Re_c = 2.8 \times 10^6$ with $[54|12]$ roughness. Here the 12 mm crossflow waves produced by the roughness array are supercritical; without artificial
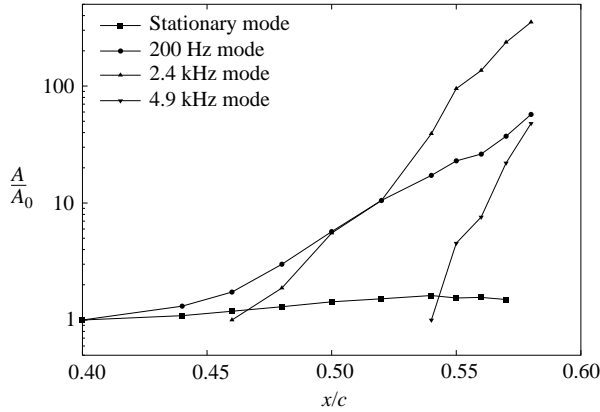
FIGURE 29. Velocity-fluctuation r.m.s. growth, $Re_c = 2.0 \times 10^6$, $[54|12]$ roughness.
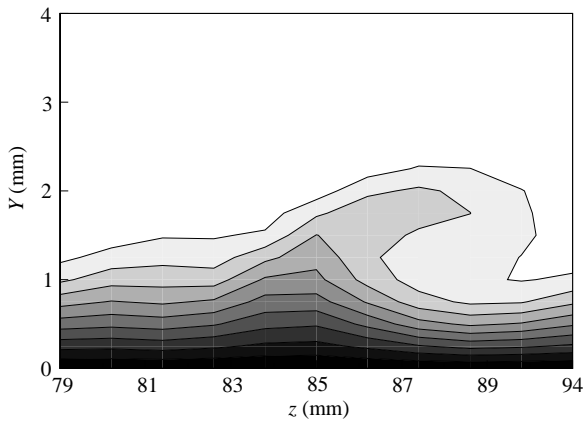

FIGURE 30. Mean-flow velocity contours, $Re_c = 2.8 \times 10^6$, $[54|12]$ roughness, $x/c = 0.30$, contour lines at $U/U_{\text{edge}} = 0.10, 0.20, \ldots, 0.90$.

roughness a 10.2 mm wave would dominate. The data presented for this case begin at $x/c = 0.30$, where the secondary instability is first detected. What is immediately apparent from the mean-flow contour plot (figure 30) is that short-wavelength harmonics of the 12 mm mode are quite important for this configuration. To the left of the low-momentum upwelling, there is a distinct plateau without a strong $\partial U/\partial z$ gradient. At first glance, this suggests that the mode-I instability may not be as important in this case as in the previous cases because its production mechanism, the $\partial U/\partial z$ gradient, is suppressed in the region in which it could be most strongly amplified. Instead, a type-II mode may play a more important role.

For this case, 300 Hz is representative of the most amplified travelling crossflow wave and 3.6 kHz is representative of the mode-I instability. Distributions of these two modes are given in figure 31. The shape of the 300 Hz mode is somewhat different from the shapes that occur for critical and subcritical forcing; here there are distinct maxima within the structure. The highest amplitudes occur just to the right of the low-momentum upwelling region as in the previous cases, but the region near the wall to the left of the upwelling also contains significant low-frequency fluctuations, as does the upper part of the overturning region. Although the highest amplitude
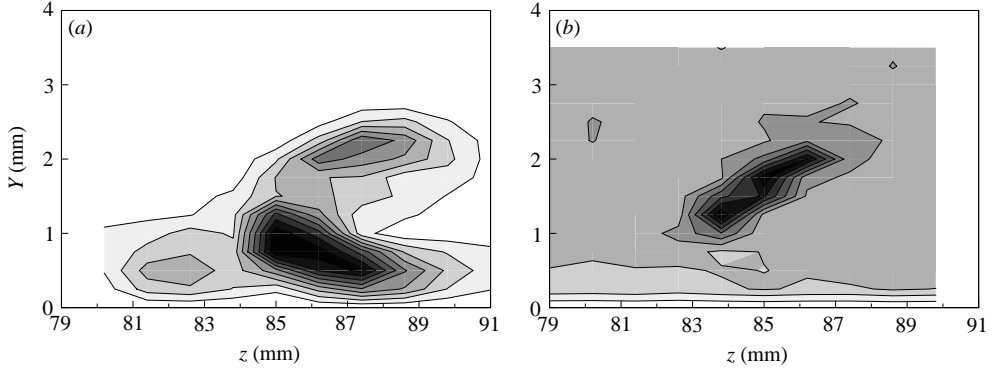
FIGURE 31. (a) 300 Hz and (b) 3.6 kHz velocity-fluctuation r.m.s. distribution, $Re_c = 2.8 \times 10^6$, $[54|12]$ roughness, $x/c = 0.30$, 200 Hz bandpass. Lines are 10% contours of the maximum in each band.
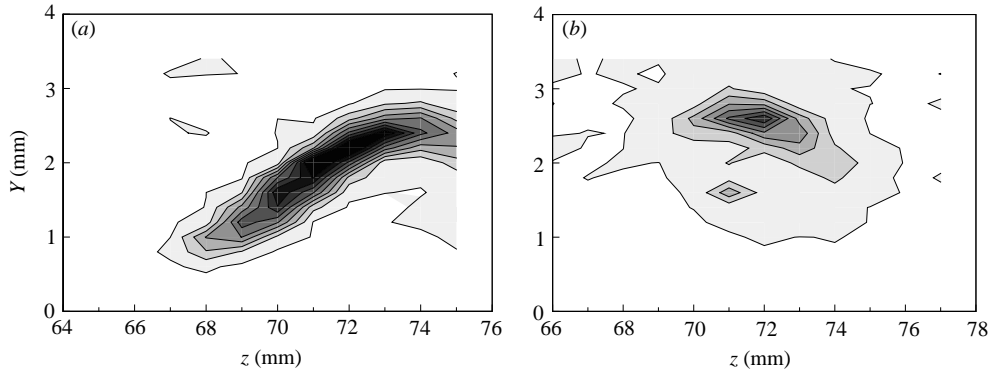

FIGURE 32. (a) 3.6 kHz and (b) 6.5 kHz velocity-fluctuation r.m.s. distribution, $Re_c = 2.8 \times 10^6$, $[54|12]$ roughness, $x/c = 0.35$, 200 Hz bandpass. Lines are 10% contours of the maximum in each band.

part of the structure occurs at roughly the same span position as in previous cases, it is somewhat lower in the boundary layer and is elongated in span. The 3.6 kHz mode is barely detectable over the background fluctuations, but it can be identified as a type-I mode based on its location within the stationary structure.

Downstream at $x/c = 0.35$, the mean flow has a character similar to the mean flow at $x/c = 0.30$. Spectra indicate that while the secondary instability has grown significantly, it does not exist as close to the surface on the left side of the stationary structure as it does in the other cases without supercritical roughness forcing. The minor lobes of the 300 Hz mode have disappeared by this station, but it retains the elongated shape seen at $x/c = 0.30$. Figure 32(a) confirms that the 3.6 kHz mode is not close to the wall and is in fact creeping along the stationary structure into the region occupied by the type-II instability. A type-II mode is detected at 6.5 kHz and is shown in figure 32(b). By $x/c = 0.37$, the peak amplitude of the 6.5 kHz type-II mode is nearly equal to the peak amplitude of the 3.6 kHz type-I mode, despite having started growing farther downstream. Mode II is more highly amplified, confirming the expectation that supercritical forcing can suppress the mode-I instability in favour of the mode-II instability.
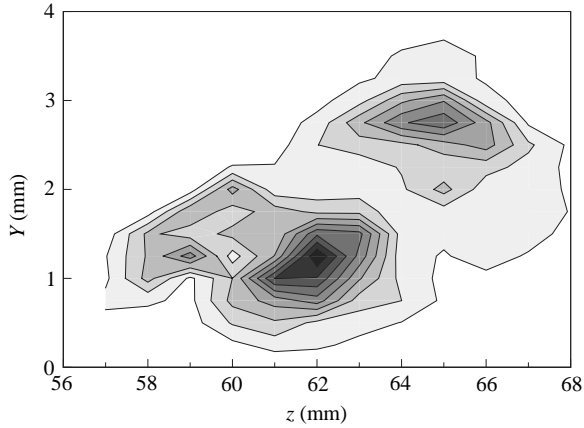
FIGURE 33. Total velocity-fluctuation r.m.s. distribution, $Re_c = 2.8 \times 10^6$, $[54|12]$ roughness, $x/c = 0.385$, 20 Hz–12.0 kHz bandpass. Lines are 10% contours of the maximum r.m.s. fluctuations.
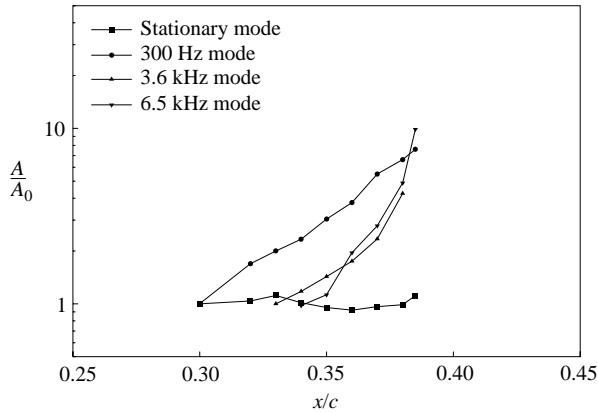

FIGURE 34. Velocity-fluctuation r.m.s. growth, $Re_c = 2.8 \times 10^6$, $[54|12]$ roughness.

Breakdown is observed at $x/c = 0.385$. The mean-flow contours do not appear markedly different and only the spectra above the low-momentum upwelling indicate that this location has undergone breakdown. The total r.m.s. fluctuations for this location are given in figure 33; and for this distribution, they indicate that the amplitude of the mode-II secondary instability is nearly as large as the low-frequency mode.

Disturbance growth curves for the $Re_c = 2.8 \times 10^6$ case are given in figure 34. This figure shows that even though the travelling waves are of somewhat higher amplitude, breakdown occurs almost immediately following the appearance of the secondary modes. The growth of the secondary-instability modes is the lowest seen in any of the experiments, but the secondary instability still appears to be a critical factor leading to breakdown. The most interesting feature of this case is the confirmation that the mode-II instability has a higher growth rate than the mode-I instability for this level of supercritical forcing because of the modified characteristic of the underlying mean flow.

3.5. *Effect of increased free-stream fluctuations*

If one is to claim that the secondary instability is the dominant feature leading to breakdown of the laminar boundary layer, an important piece of supporting evidence could be that an increase in the initial secondary-instability amplitude leads directly to accelerated breakdown. Two means of introducing such an increase are attempted: free-stream acoustic forcing and enhanced free-stream turbulence. In both cases, the idea is to choose a location just upstream of the breakdown location and observe whether the introduction of an increased initial disturbance amplitude at the secondary-instability frequencies moves the transition location upstream. A measurement location just upstream of breakdown is used because this position includes the integrated effect of the entire instability process, and if there is to be any effect of enhanced initial amplitude, it will be most obvious here. Detection of a positive result would then prompt more detailed measurements.

The experimental results of Radeztsky *et al.* (1999) would tend to discount the likelihood of observing such a result for acoustic forcing, since in those experiments no effect on transition was observed with up to 95 dB acoustic forcing at various frequencies, including the secondary instability frequency range. However, those experiments were conducted without periodic leading-edge roughness and hence with a lower-amplitude, less-organized stationary-disturbance state. Use of acoustic forcing with periodic roughness might yield a different result. Also, because the secondary instability grows so rapidly, even a significant increase in its initial amplitude might not be manifested in a dramatic change in the transition location. Because breakdown occurs within a few percent chord of where the secondary modes destabilize, an increase in the initial amplitude could at most move the transition location upstream by this same few percent chord. Because the change in transition location could be quite subtle, it is not clear that this would have been detected in the previous experiment, because at that time, the details that we now understand regarding the secondary-instability growth were not known.

Acoustic forcing is more straightforward than turbulence forcing because it simply requires activating speakers in the plenum upstream of the test section during an experiment. This means that it is possible to obtain high and low acoustic levels during a single run without any experimental hardware changes. Two tests are conducted, both with $[54|12]$ roughness. The first test is conducted at $Re_c = 2.4 \times 10^6$ with the hot-wire probe located at $x/c = 0.39$, $z = 86$–89 mm, the location of maximum secondary-instability activity. At these locations, sound frequencies between 2.0 and 4.0 kHz are applied at the maximum amplitude available in the facility, 125 dB. At frequencies above 2.8 kHz, the sound amplitude decreases significantly due to the capability of the speakers (woofers designed for frequencies in the 100s of Hz). For the entire range of secondary-instability frequencies, no change in the velocity-fluctuation spectra is observed at any position within the stationary-vortex structure at the 39% chord position. The second test is conducted at $Re_c = 2.0 \times 10^6$ with the hot wire at $x/c = 0.55$, $z = 88$ mm (see figures 25 and 27). These conditions are better suited to the objective because the mode-I secondary instability is centred near 2.4 kHz, within the capability of the speakers, and because the maximum amplitude of the secondary instability is much greater than the surrounding frequency band, so the spectral signal is unambiguous. However, as with the higher Reynolds number case, maximum-amplitude acoustic input from 1.5–3.0 kHz has no discernible effect on the boundary layer.

To assess the effect of free-stream turbulence, a small turbulence-generating grid is positioned in the contraction cone upstream of the test section. The grid produces

$u'_{\text{r.m.s.}}/U_\infty$ as high as 0.29%, high enough that travelling-wave-dominated flow might result. Spectra of the u' in the free-stream are flat up to about 800 Hz and roll off thereafter, reaching the electronic noise floor by 4 kHz. Tests at all three chord Reynolds numbers are performed with the turbulence grid in place. In all cases the travelling waves are enhanced, but in no case does the transition location change, and no changes are detected in the behaviour of the secondary instability. The fundamental problem with this approach is applying high-frequency turbulence without also inducing the low-frequency content that will produce overwhelmingly large travelling crossflow waves and change the nature of the primary instability from stationary- to travelling-wave dominated.

These tests underscore a fundamental difficulty associated with boundary-layer-stability experiments. One must always consider receptivity when attempting a controlled means of forcing an instability. For secondary instabilities, the problem is even more pronounced. Here, the receptivity encompasses both the initial entrainment of the free-stream disturbance of the desired frequency and the subsequent evolution of that mode until the secondary instability becomes amplified.

4. Conclusions

This experiment is intended to provide conclusive data regarding the breakdown mechanism of crossflow-dominated swept-wing boundary layers: a rapidly growing high-frequency secondary instability of the stationary crossflow vortices. The secondary-instability modes observed in this experiment are destabilized once the primary crossflow waves reach high amplitudes and grow much more rapidly than the low-frequency mode that has its origins in the most amplified travelling crossflow wave predicted by linear theory. Local breakdown is always observed within a few percent chord of where the secondary instability is first detected. The data presented here overwhelmingly support the idea that the secondary instability, perhaps in combination with the low-frequency fluctuations, is responsible for breakdown. Additionally, the results confirm the DNS of Wassermann & Kloker (2002) that shows transition not to be the result of an absolute instability.

The secondary-instability modes that are observed may be classified as either type-I or type-II modes. The type-I modes lie inboard of the low-momentum upwelling zone of the stationary crossflow vortices and occur under a wider range of conditions than the type-II modes. The type-II modes are located high in the boundary layer above and somewhat outboard of the upwelling zone. Both types are inflectional instabilities of streamwise flow. Type-I modes are driven primarily by a $\partial U/\partial z$ gradient, whereas the type-II modes are driven primarily by a $\partial U/\partial Y$ gradient. The more-frequent appearance of the type-I mode is similar to behaviour observed by Swearingen & Blackwelder (1987) for secondary instabilities of Görtler vortices for which spanwise shear layers are more effective than wall-normal shear layers at producing secondary instabilities.

The type-I mode extends diagonally in the (Y, z)-plane and can be imagined as wrapping around the outside of this portion of the stationary vortex. This is the behaviour shown very clearly in the rotating-disk flow visualizations of Kohama (1984, 1985) and in the DNS studies of Wassermann & Kloker (2002). In nearly all circumstances, the lowest-frequency secondary instability is a type-I mode and is the highest-amplitude mode that is detected. In many instances, one or more higher-frequency type-I modes coexist at the same location. These are observed at close to integer multiples of the lowest-frequency type-I mode. Although this strongly suggests

that the higher frequencies are harmonics of the dominant mode, the growth rates do not always support this. These results also show that to properly understand the breakdown region in as much detail as possible, narrow frequency bands should be investigated separately. As many as five or more instability modes exist in some cases, so tracking the behaviour of bands as wide as a kilohertz or more can lump the behaviour of many modes into a single result.

In cases where it is observed, the type-II mode is about twice the frequency of the highest-amplitude type-I mode. It is often overwhelmed by the growth of the (possible) harmonic of the fundamental type-I mode and is therefore extremely difficult to track experimentally. One exception is the supercritical forcing case, $Re_c = 2.8 \times 10^6$ with $[54|12]$ roughness. For this configuration, the spanwise shear region is reduced and the type-I modes do not reach the amplitude that they do under more favourable conditions. In this environment, the type-II mode is detected more easily and plays an important role in triggering transition.

It is worth noting that Li & Malik (1995) observed exactly the same selection mechanism in simulations of Görtler vortices. Li & Malik find that when the primary mode's wavelength is small and the spanwise gradients are large the dominant secondary instability is the sinuous mode that is located on the sides of the Görtler vortex. If the wavelength of the primary instability is increased then the horseshoe mode located on top of the vortex dominates. This is exactly parallel to what is observed here. The type-I mode located on the side of the vortex dominates when the primary wavelength is subcritical (short) and the type-II mode that is located on top of the vortex dominates when the vortex spacing is supercritical (large).

Although the low-frequency fluctuations that correspond to the most amplified primary disturbance are not the focus here, their behaviour is interesting and would be a useful topic of further study. The low-frequency fluctuations begin as a spanwise-uniform mode at chord locations where mean flow is not yet deformed by the stationary vortices. However, these fluctuations become highly localized within the stationary structure even before the stationary mode saturates. Despite the modification of the mean flow and the spatial redistribution of the low-frequency mode that results, these modes appear to grow linearly throughout transition.

Comparing the $[54|12]$ and $[18|12]$ roughness cases at $Re_c = 2.4 \times 10^6$ indicates that an increase in roughness amplitude increases the amplitude of the low-frequency mode. However, even when the low-frequency fluctuations are quite large, breakdown does not occur until the secondary instability is destabilized. In the higher-amplitude-roughness case it is not possible to say whether the secondary instability alone or some combination of the low- and high-frequency disturbances leads to breakdown. However, breakdown always occurs within a few percent chord of where the secondary instability destabilizes. Therefore, the secondary instability always appears to be important but the low-frequency fluctuations may only be important in some cases. An attempt was made to accelerate transition using free-stream sound and enhanced free-stream turbulence but these efforts were unsuccessful because of the difficulty of directly exciting the secondary instability.

Taken as a whole, the experiments demonstrate the range of behaviours that are exhibited by the secondary instability and emphasize that to predict transition location in crossflow boundary layers, one must be capable of predicting secondary-instability behaviour. What we have seen is that the most important factor for the secondary instability is the wavelength of the stationary disturbances. Different wavelengths, and their classification as subcritical, critical, or supercritical, play an important role in selecting the dominant secondary-instability mode, either type I

or type II. Previous experiments have shown that roughness amplitude may not be important for determining transition location because of amplitude saturation. That idea is extended here by noting that increased roughness amplitudes increase the amplitudes of low-frequency disturbances, but these do not appear to trigger breakdown independently. This may not be so for low-frequency disturbances of larger amplitudes than are produced in this experiment, but the low-disturbance environment is more representative of flight and therefore represents the most important practical case. In the low-disturbance environment, breakdown always appears to require secondary-instability growth.

REFERENCES

ARNAL, D. 1997 Laminar-turbulent transition: Research and applications in France. *AIAA Paper* 97–1905.

BIPPES, H. 1999 Basic experiments on transition in three-dimensional boundary layers dominated by crossflow instability. *Prog. Aero. Sci.* **35**, 363–412.

CHAPMAN, K. L., REIBERT, M. S., SARIC, W. S. & GLAUSER, M. N. 1998 Boundary-layer transition detection and structure identification through surface shear-stress measurements. *AIAA Paper* 98–0782.

CROUCH, J. 1997 Transition prediction and control for airplane applications. *AIAA Paper* 97–1907.

DAGENHART, J. R. & SARIC, W. S. 1999 Crossflow stability and transition experiments in swept-wing flow. *NASA TP* 1999-209344. Originally appeared as a Virginia Polytechnic Institute PhD thesis by Dagenhart, 1992.

DEYHLE, H. & BIPPES, H. 1996 Disturbance growth in an unstable three-dimensional boundary layer and its dependence on initial conditions. *J. Fluid Mech.* **316**, 73–113.

FISCHER, T. M. & DALLMANN, U. 1991 Primary and secondary stability analysis of a three-dimensional boundary layer. *Phys. Fluids* A **3**, 2378–2391.

HAYNES, T. S. & REED, H. L. 2000 Simulation of swept-wing vortices using nonlinear parabolized stability equations. *J. Fluid Mech* **405**, 325–349.

HERBERT, TH. 1997a On the stability of 3-D boundary layers. *AIAA Paper* 97–1961.

HERBERT, TH. 1997b Transition prediction and control for airplane applications. *AIAA Paper* 97–1908.

HÖGBERG, M. & HENNINGSON, D. 1998 Secondary instability of crossflow vortices in Falkner–Skan–Cooke boundary layers. *J. Fluid Mech.* **368**, 339–357.

JANKE, E. & BALAKUMAR, P. 2000 On the secondary instability of three-dimensional boundary layers. *Theoret. Comput. Fluid Dyn.* **14**, 167–194.

KACHANOV, Y. S. 1996 Experimental studies of three-dimensional instability of boundary layer. *AIAA Paper* 96–1976.

KAWAKAMI, M., KOHAMA, Y. & OKUTSU, M. 1999 Stability characteristics of stationary crossflow vortices in three-dimensional boundary layer. *AIAA Paper* 99–0811.

KOCH, W., BERTOLOTTI, F. P., STOLTE, A. & HEIN, S. 2000 Nonlinear equilibrium solutions in a three-dimensional boundary layer and their secondary instability. *J. Fluid Mech.* **406**, 131–174.

KOHAMA, Y. 1984 Study on boundary layer transition of a rotating disk. *Acta Mechanica* **50**, 193–199.

KOHAMA, Y. 1985 Turbulent transition process of the spiral vortices appearing in the laminar boundary layer of a rotating cone. *PhysicoChemical Hydrodyn.* **6**, 659–669.

KOHAMA, Y. 1987 Some expectations on the mechanism of cross-flow instability in a swept-wing flow. *Acta Mechanica* **66**, 21–38.

KOHAMA, Y. & EGAMI, Y. 1999 Active control of instabilities in a laminar boundary layer. *AIAA Paper* 99-0921.

KOHAMA, Y., ONODERA, T. & EGAMI, Y. 1996 Design and control of crossflow instability fiield. In *IUTAM Symposium on Nonlinear Instability and Transition in Three-Dimensional Boundary Layers* (ed. P. Duck & P. Hall), pp. 147–156. Kluwer.

KOHAMA, Y., SARIC, W. S. & HOOS, J. A. 1991 A high-frequency, secondary instability of cross-flow vortices that leads to transition. In *Proc. Royal Aero. Soc. Conf. on Boundary-Layer Transition and Control*.

LERCHE, T. 1996 Experimental investigation of nonlinear wave interactions and secondary instability in three-dimensional boundary-layer flow. In *6th European Turbulence Conference, Lausanne* (ed. S. Gavrilakis, L. Machiels & P. A. Monkewitz), pp. 357–360. Kluwer.

LERCHE, T. & BIPPES, H. 1996 Experimental investigation of cross-flow instability under the influence of controlled disturbance excitation. In *Transitional Boundary Layers in Aeronautics* (ed. R. A. W. M. Henkes & J. L. van Ingen). North Holland.

LI, F. & MALIK, M. R. 1995 Fundamental and subharmonic secondary instabilities of Görtler vortices. *J. Fluid Mech.* **297**, 77–100.

MALIK, M. R., LI, F. & CHANG, C.-L. 1994 Crossflow disturbances in three-dimensional boundary layers: Nonlinear development, wave interaction and secondary instability. *J. Fluid Mech.* **268**, 1–36.

MALIK, M. R., LI, F. & CHANG, C.-L. 1996 Nonlinear crossflow disturbances and secondary instabilities in swept-wing boundary layers. In *IUTAM Symp. on Nonlinear Instability and Transition in Three-Dimensional Boundary Layers* (ed. P. W. Duck & P. Hall), pp. 257–266. Kluwer.

MALIK, M. R., LI, F., CHOUDHARI, M. M. & CHANG, C.-L. 1999 Secondary instability of crossflow vortices and swept-wing boundary layer transition. *J. Fluid Mech.* **399**, 85–115.

POLL, D. I. A. 1985 Some observations of the transition process on the windward face of a long yawed cylinder. *J. Fluid Mech.* **150**, 329–356.

RADEZTSKY, JR., R. H. 1994 Growth and development of roughness-induced stationary crossflow vortices. PhD thesis, Arizona State University.

RADEZTSKY, JR., R. H., REIBERT, M. S. & SARIC, W. S. 1999 Effect of isolated micron-sized roughness on transition in swept-wing flows. *AIAA J.* **37**, 1371–1377.

REED, H. L. & SARIC, W. S. 1989 Stability of three-dimensional boundary layers. *Annu. Rev. Fluid Mech.* **21**, 235–284.

REIBERT, M. S., SARIC, W. S., CARRILLO, JR., R. B. & CHAPMAN, K. L. 1996 Experiments in nonlinear saturation of stationary crossflow vortices in a swept-wing boundary layer. *AIAA Paper* 96–0184.

RESHOTKO, E. 1997 Progress, accomplishments and issues in transition research. *AIAA Paper* 97–1815.

SARIC, W. S. 1992 The ASU transition research facility. *AIAA Paper* 92–3910.

SARIC, W. S., CARRILLO, JR., R. B. & REIBERT, M. S. 1998 Nonlinear stability and transition in 3-D boundary layers. *Meccanica* **33**, 469–487.

SARIC, W. S., REED, H. L. & WHITE, E. B. 2003 Stability and transition of three-dimensional boundary layers. *Annu. Rev. Fluid Mech.* **35**, 413–440.

SWEARINGEN, J. D. & BLACKWELDER, R. F. 1987 The growth and breakdown of streamwise vortices in the presence of a wall. *J. Fluid Mech.* **182**, 255–290.

WASSERMANN, P. & KLOKER, M. 2002 Mechanisms and passive control of crossflow-vortex-induced transition in a three-dimensional boundary layer. *J. Fluid Mech.* **456**, 49–84.

WHITE, E. B. 2000 Breakdown of crossflow vortices. PhD thesis, Arizona State University.

WINTERGERSTE, T. & KLEISER, L. 1996 Direct numerical simulation of transition in a three-dimensional boundary layer. In *Transitional Boundary Layers in Aeronautics* (ed. R. A. W. M. Henkes & J. L. van Ingen). North Holland.